Characteristics of desert varnish from nanometer to micrometer scale: A photo-oxidation model on its formation

Xiaoming Xu[a], Yan Li[a,*], Yanzhang Li[a], Anhuai Lu[a,*], Ruixi Qiao[b], Kaihui Liu[b], Hongrui Ding[a], Changqiu Wang[a]

[a] The Key Laboratory of Orogenic Belts and Crustal Evolution, Beijing Key Laboratory of Mineral Environmental Function, School of Earth and Space Sciences, Peking University, Beijing 100871, China
[b] School of Physics, Peking University, Beijing 100871, China

ARTICLE INFO

ABSTRACT

Rock varnish is a widespread Mn-rich rock coating commonly developed in arid environments, but the mechanism for its formation is still under debate. In this study, rock varnish and adjacent soil dust collected from Gobi Desert were analyzed for exploring the possible abiotic oxidation mechanism of Mn oxides. The occurrence of rock varnish shows a direct and close relationship with strong irradiation of sunlight, giving the first evidence of photochemical genesis. Abundant caves and tunnels with average diameter of ~1–5 μm are observed on varnish surface regions, which facilitate the penetration of sunlight and water. Metal (oxyhydr)oxides, including birnessite, hematite, goethite, rutile and anatase, account for the major components of rock varnish, which are all solar light-responsive semiconducting minerals. The trace elements enrichment patterns revealed by LA-ICP-MS provide the indication of an aqueous origin. The positive Ce anomalies in varnish in contrast to the rock substrate, as well as the positive correlation between Ce and Mn suggest a strong oxidizing environment in the genesis of rock varnish. Therefore, the photo-generated holes and reactive oxygen species (ROSs) on metal oxides in varnish can promote Mn(II) oxidation, which are further demonstrated from thermodynamic and kinetic considerations. ROSs including $^1O_2$ and OH· with strong oxidizing capability are detected by EPR in varnish suspension, providing the direct evidence for Mn(II) oxidation. Laboratory experimental simulations show the photocatalysis of metal oxides in rock varnish greatly promote Mn(II) oxidation by 2.10–7.97 times in comparison with homogenous solution oxidation. All these lines of evidence suggest that light-induced abiotic process may play important roles in the formation of rock varnish together with other abiotic and biotic pathways, which can even provide implications for the evolution of Mn oxides on surface of terrestrial planets.

1. Introduction

Rock varnish is one of the most representative Mn deposits in terrestrial weathering environments, covering the rock surface of a diversity of lithologies (Engel and Sharp, 1958; Dorn, 1991, 2007). It is mainly composed of poorly crystallized Mn oxides, Fe oxides and clay minerals (Potter and Rossman, 1977, 1979a) with limited content of other mineral clasts and organic matters (Dorn and Oberlander, 1982; Dorn, 1998; Mancinelli et al., 2002; Edwards et al., 2004; Malherbe et al., 2015). The clay minerals occupy 70% of rock varnish volume and consist of illite and montmorillonite, cemented by the nanocrystalline matrix of Mn/Fe oxides on the substrate surface (Potter and Rossman, 1977). Fe oxides in rock varnish is mainly hematite while birnessite is the dominant phase of Mn oxides, together with a small fraction of large

tunnel structured Mn oxides including todorokite and romanechite (Potter and Rossman, 1979a; McKeown and Post, 2001; Garvie et al., 2008; Xu et al., 2018). The most distinct geochemical feature of rock varnish is the Mn enrichment, which is ~50–200 times of the value in upper continental crust (Thiagarajan and Lee, 2004; Goldsmith et al., 2014).

Rock varnish commonly displays layered structure and botryoidal structure, in which more sophisticated microlaminations can be discovered (Perry and Adams, 1978). These microlayers serve as potential environmental indicators for paleoclimate (Krinsley et al., 1995) and effective dating tools for geological sites (Liu, 2003; Liu and Broecker, 2007). The thickness of rock varnish displays great fluctuation, ranging from tens to hundreds of micrometers (Liu and Broecker, 2000; Northup et al., 2010) with a slow growth rate of 1–40 μm per 1000 year (Liu and

---

Broecker, 2000). Other researches show the growth can be much faster for the topmost part of rock varnish (Spilde et al., 2013).

Since the first description of rock varnish written by Alexander Von Humboldt and Bonpland (1819) who observed it in the splash zone at the cataracts of the Orinoco River, much interest has been paid to this field and many works have been published about rock varnish from different sites, including arid desert (Dorn, 2009; Goldsmith et al., 2014), urban areas (Vicenzi et al., 2016), high mountains (Dorn, 1991), cold environments (Dorn et al., 1992) and even extraterrestrial sites (DiGregorio, 2001; Perry and Kolb, 2004a; Lanza et al., 2012). However, so far the precise formation mechanism of rock varnish remains highly controversial and unsolved. The key concerns of a proper formation theory should include the materials source and oxidation mechanisms of Mn(II) to form Mn oxides in rock varnish. The general structure of Mn oxides and hydroxides is MnO_6 octahedrons sharing corners or edges with each other, thus forming chain, tunnel, and sheet structures (Post, 1999). Which kind of Mn oxides and hydroxides form depends on many factors, such as pH, Eh, temperature, cation availability, etc. (Hem, 1972; Brookins, 1988; McKeown and Post, 2001). However, Mn (oxyhydr)oxides are famous for their fine grains and poor crystallinity. Additionally, vacancies, mixed valence states of Mn and substitution of foreign cations in Mn (oxyhydr)oxides make them in rock varnish very hard to characterize, thus with complicated and confusing origin hypothesis.

So far three main theories of varnish formation have been proposed (Dorn, 2007, 2008): 1) Abiotic hypothesis (Engel and Sharp, 1958; Smith and Whalley, 1988; Thiagarajan and Lee, 2004; Goldsmith et al., 2014). This theory relies on the greater mobility of divalent manganese over ferrous iron under small pH fluctuations. The Mn released from dust by slightly acid rainwater or dew (pH < 6.5) is then fixed in clays after water evaporation which can give rise to a pH condition > 8.5. However, this fixation process is very slow in kinetic considerations and is contradictory to geographical distribution of varnish, i.e., varnish in wetter climates are typically higher in Mn content than those in arid, more alkaline settings (Dorn, 2007). 2) Biotic hypothesis (Dorn and Oberlander, 1981; Perry and Kolb, 2004a; Perry et al., 2004; Northup et al., 2010). This theory underlines the interaction between microorganisms and surrounding inorganic world. The metabolites provide a Mn accumulation nucleation center followed by subsequent growth. However, biogenic Mn oxidation is much faster when compared with abiogenic oxidation, which contradicts the real varnish formation rate of 1–40 μm per 1000 year (Liu and Broecker, 2000). 3) Polygenetic model (Dorn, 2007). This theory is a combination of the processes described above. Wetting effect on soil dust provides materials source and weathered remains of Mn-rich bacterial casts cement clay minerals to rock surfaces.

In the current hypotheses about varnish formation, the sunlight factor that the rock surface has been influenced for billions of years was almost neglected. With the continuous and strong irradiation of sunlight on rock surface, abiotic photochemical processes are very likely to happen during the formation of varnish. Therefore, we conducted detailed field investigation and mineralogical analysis on desert varnish samples, as well as laboratory simulation experiments on photochemical formation of Mn oxides, thus to verify our hypothesis. Our goal is to provide a comprehensive understanding and new insights towards the abiotic genesis of rock varnish, and even implications for the evolution of Mn oxides on terrestrial planet surface.

2. Materials and methods

2.1. Sample collection

Rock varnish was collected from the Gobi Desert in Hami city, Xinjiang province, which is located south to the Tianshan Mountains. Specific sample locations are listed in Table 1. Varnish samples were impregnated and solidified using polyester resin, cut along the vertical

Table 1
Sampling site locations and description.

Site name	Location	Topography
GD-1	43°17′47″N 92°16′58″E	Alluvial fan
GD-2	43°19′10″N 92°14′51″E	Alluvial fan
GD-3	43°21′04″N 92°12′52″E	Alluvial fan
GD-4	43°0′25″N 93°41′08″E	High hills
GD-5	43°15′39″N 92°21′02″E	Alluvial fan

direction of coating surface into the substrate and then burnished into thin sections with thickness of ~30 μm. Thin sections were observed under optical microscope (OP) in transmission light mode. Smooth micro-basins (depth/width ≈ 1/3) on the rock varnish samples were chosen for the preparation of varnish powders, since the varnish here can be thicker than rough surfaces and incorporation of substrate composition can be avoided. We scraped the surface of varnish in the laboratory and prepared fine-grained powders using a high-purity quartz rod.

Aeolian dust has been considered to be the major source material of rock varnish (Potter and Rossman, 1977; Krinsley, 1998; Garvie et al., 2008). Dust samples adjacent to varnished rocks were also collected for comparative research of chemical composition using a stainless-steel spoon. The dust grains passed through a 500-mesh sieve in the laboratory to yield a final particle size of ~25 μm. Then, samples were analyzed using an ICP-MS.

2.2. Scanning electron microscope (SEM)

Representative samples (including both thin sections and smooth varnish surface) were selected and Cr-coated for analysis using a Quanta 650 FEG field emission scanning electron microscope with X-ray energy dispersive spectroscopy (EDS) for chemical analysis. Morphological observation was conducted through both secondary electron image and back-scattered image. Experiment was carried out at an acceleration voltage of 15 kV.

2.3. Fourier transform infrared spectroscopy (FTIR)

Most Mn oxide minerals have poor crystallinity and thus are difficult to be accurately identified by XRD. FTIR is a useful technique sensitive to both long-range and short-range order materials (Potter and Rossman, 1979b). Infrared spectra of rock varnish were acquired using a Nicolet 6700 FTIR spectrometer. Data were obtained with a spectral resolution of $4 \, cm^{-1}$ across the 400–$4000 \, cm^{-1}$ wavenumber offset range. Accumulation times for the background and sample are both 16. Varnish powders were mixed with anhydrous KBr according to the mass scale of 1:100. The mixture was fully mingled and grinded in the agate mortar.

2.4. Micro-Raman spectroscopy

Micro-Raman spectra of the thin sections were acquired using a micro-Raman spectrometer (inVia Reflex, Renishaw, UK) with a laser excitation wavenumber of 785 nm to avoid fluorescence signal. Compared with traditional powder tests, micro-Raman spectra analysis conducted on varnish thin sections can exclude the interference of substrate. Initial laser power from the diode laser was 300 mW and slit width was 65 μm with 1200 line/mm grating. Spectra acquisition was performed under 50× Leica objective lens across the 100–$1300 \, cm^{-1}$ wavenumber offset range, and the spot size was 1 μm. The static grating mode was adopted during the test and integration time for individual measurement was 5 s. Accumulation times ranged from 3 to 20, which was based on the spectrum quality and signal to noise ratio. The Raman shift position was calibrated using silicon peak at $520.5 \, cm^{-1}$ with a wavenumber resolution superior to $1 \, cm^{-1}$.

2.5. Transmission electron microscope (TEM)

Since fine mineral grains in rock varnish are hardly visible under an optical microscope, transmission electron microscope coupled with X-ray energy dispersive spectroscopy equipment and selected area electron diffraction were used to provide crystallographic information of the samples from nanometer scale. Approximately 0.1 mL alcohol which contained varnish powders after ultrasonic dispersion was dripped on the inner area of a mesh copper grid (with a diameter of about 2.5 mm). The alcohol was then absorbed by the filter paper from the other side of the grid. The mesh copper grid was placed into the sample holder which was attached to the specimen stage. The experiment was carried out with a JEM-2100F transmission electron microscope, operating at 200 kV. The point resolution is 0.19 nm. The data were processed and analyzed using Digital Micrograph. EDS elements mapping was employed to locate the Mn/Fe/Ti-rich area before further characterization.

2.6. Electron probe microanalysis (EPMA)

The major elements composition of rock varnish was analyzed using a JXA 8100 electron microprobe. Thin sections were coated with C before the electron microprobe test. Elements including Na, K, Ti, Mg, Si, Mn, Al, P, Fe, Cl, Ca and Ba were measured with an acceleration voltage of 15 kV and a beam current of 10 nA. The standards employed were natural minerals from the Society of the Plastics Industry, Inc. (SPI). The diameter of a focused electron beam is ~2 μm. The peak counting time was 20 s for each element. The chemical composition of 20 randomly selected spots on different thin sections was analyzed and the weight percentage was given as oxides.

2.7. Laser ablation inductively coupled plasma mass spectrometry (LA-ICP-MS)

Rock varnish samples were analyzed using a LA-ICP-MS to acquire the minor and trace elements information. The experiment was carried out with an ESI/New Wave UP-193 Excimer laser ablation system. The ICP-MS is a VG PQ ExCell. The laser was operated in spot-drill mode at 10 Hz and the fluence is ~10.6 J/cm², under which condition the laser penetrated rock varnish but did not penetrate the underlying substrate. The spot size was 70 μm and data was collected for 50 s, in addition to 20 s of background. The data was calibrated using USGS standard NIS 610 glass. The data was processed using Glitter. Al content based on the EPMA results was chosen for chemical normalization.

2.8. Scanning transmission electron microscope (STEM) and focused ion beam (FIB) sputtering

Focused ion beam sputtering was performed using a FIB dual-beam instrument (Zeiss Auriga Compact). The sample preparation process is similar to the procedures of Krinsley et al. (2013). SEM microscopy was applied to carefully determine and monitor the site of milling. The selected preparation sites were coated with an additional, approximately 1 μm thick Pt layer. Milling was performed by Ga ion sputtering with a resolution of about 5 nm. Ultra-thin FIB sections were finally milled to sizes of about 4 × 7 μm and thickness of about 100 nm. This FIB section was later placed on a Cu TEM grid. Scanning transmission electron microscope analysis and EDS mapping were conducted to study its structure and elements distribution patterns on nanometer scale.

2.9. Electron paramagnetic resonance (EPR) spectroscopy

The EPR measurements were carried out with an EMXplus-6/1 EPR spectrometer (Bruker) operating at X-band frequencies. Signals of solid varnish powders were detected. The rock varnish powders were inserted into a glass tube which was later introduced to the EPR

Table 2
Specific surface areas (SSAs) of different minerals determined by BET method.

Minerals	Goethite	Hematite	Anatase	Rutile
BET surface area (m²/g)	82.52	4.18	30.11	31.09

instrument. Signals of ROSs produced by varnish powders in aqueous system were also obtained by EPR instrument. Varnish suspension was prepared and transferred to a glass tube. DMPO (5,5-dimethyl-1-pyrroline-N-oxide) was added into the suspension as a radical scavenger. The solution was irradiated from the side by a xenon lamp (CEL-HXF300, AULTT, China) with an output energy of 50 W/cm² at a distance of 20 cm. All experiments were carried out at room temperature (~293 K) and the frequency was 9.83 GHz. The magnetic field was scanned from 0 to 6000 G.

2.10. Laboratory experiments of abiotic oxidation of Mn(II)

Synthetic standard minerals including goethite, hematite, anatase and rutile were purchased from Alfa Aesar (Ward Hill, Massachusetts, USA). The specific surface areas (SSAs) of different minerals were determined by BET method (Table 2). The X-ray diffraction (XRD) analysis was conducted to guarantee these samples in pure phase.

A 150 mL solution with initial Mn(II) concentration of 14 mM was prepared in a 250 mL quartz vessel. To keep the same total surface area of each mineral in vessel, 0.38 g goethite, 7.44 g hematite, 1.03 g anatase and 1 g rutile was separately added to the solution and dispersed by sonication for ~5 min. After mixture, the Mn(II) was oxidized at pH 7, 25 °C with a continuous flow rate of 0.15 m³/h air for 8 h under constant stirring. The suspension was irradiated from the side by a xenon lamp (CEL-HXF300, AULTT, China) with an output energy of 50 W/cm² at a distance of 10 cm. During the reaction, a 1.5 mL suspension was taken out every 1 h, and the Mn(III/IV) content was quantified using colorimetric dye Leucoberbelin blue (LBB) (Krumbein and Altmann, 1973; Francis et al., 2001). The suspension was mixed with 0.5 mL LBB. After complete reaction of 40 min, the solution and solid phase were quickly separated from each other by a 0.22 μm membrane filter. The absorbance of the supernatant was measured at 620 nm on a UV–Vis spectrophotometer (Thermo Fisher Scientific, USA). Standard curves were obtained using LBB mixed with different amounts of $KMnO_4$, as described by Francis et al. (2001). The 1 mM $KMnO_4$ is equivalent to 5 mM trivalent Mn oxides or 5/2 tetravalent Mn (oxyhydr)oxides through the equivalent electron transfer from LBB to Mn(III) or Mn(IV) in Mn(III/IV) (oxyhydr)oxides to form Mn(II).

Two control experiments were conducted with one group operated in dark system and the other in the absence of metal oxide minerals. The experimental conditions and procedures were the same as described above. All experiments were repeated three times for each semiconducting mineral. The standard deviation of three individual experiments was used as the error bar.

3. Results

3.1. Field occurrence of rock varnish

Field investigation shows varnish grows on host rock pebbles. The pebbles spread on the desert pavement demonstrating black varnish curst with metallic luster on their top (Fig. 1a), while the part close to the pebbles rim is dull brown (Fig. 1b). The bottom, ground-facing side of pebbles shows red stains but no varnish (Fig. 1b). This phenomenon indicates that black and red coloration grows from the rock-soil-atmosphere contact towards rock surface and subsoil, respectively. Furthermore, black varnish is also observed on the topmost part of rock cracks with depth of several centimeters (Fig. 1c & d). The bottom of the crack is filled with dust which contributes to the khaki color of the
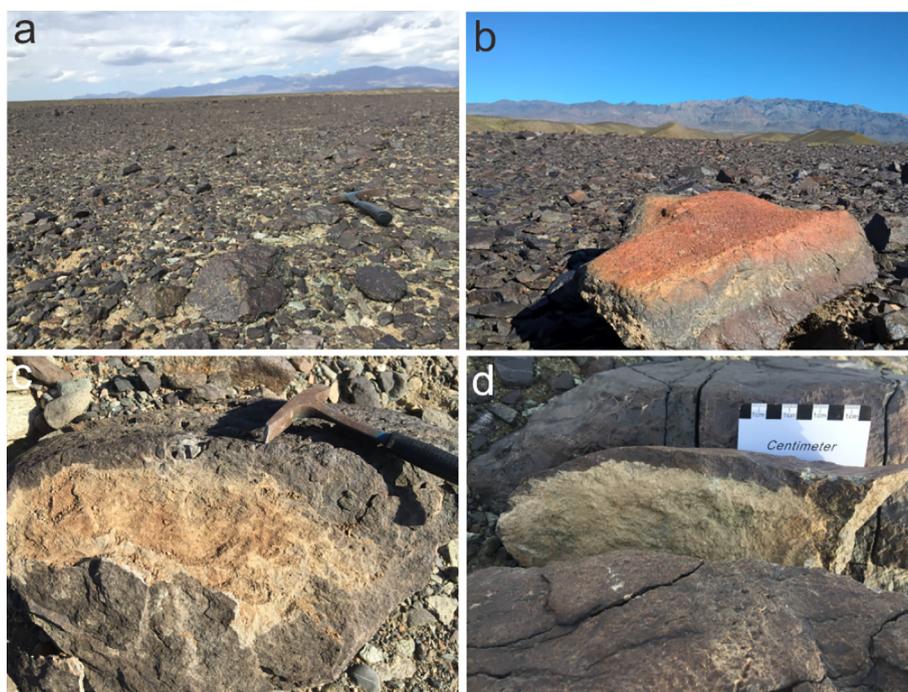
Fig. 1. Field observation of rock varnish in Gobi Desert. Varnish develops on the surface of pebbles (a, b) and side face of rock cracks (c, d). Its occurrence shows close relationship with solar light.

lower part of crack (Fig. 1c). The occurrence of rock varnish shows close relationship with the irradiation of solar light.

3.2. Morphology of rock varnish

Under optical microscope, the varnish develops layered structure with thickness of 25–150 μm (Fig. 2a & b), which covers a diversity of lithologies including granite, basalt and quartzite. The boundary between varnish and underlying substrate is very distinct. Varnish can extend to several millimeters bilaterally and show much resemblance with stromatolite-like structure, i.e., alternating dark and light layers can be discriminated and the thickness of each layer is only ~2–5 μm (Fig. 2a & b). Previous researches indicated that the color contrast arose from different contents of Mn oxides (Perry and Adams, 1978), which are the dominant pigmenting agent in varnish.

Secondary electron images indicate the surface of rock varnish is uneven (Fig. 2c). Small caves with diameter of ~5 μm are common on the surface, which may be formed by the erosion of acid rainfalls or metabolites produced by microorganisms (Fig. 2d). Back-scattered images of thin sections also demonstrate clear boundary between varnish and substrate (Fig. 2e). Besides, the varnish part exhibits lighter color than the substrate, indicating its enrichment of heavier elements. The cross profile of rock varnish is loose and porous (Fig. 2f). Mineral grains physically wrapped by the accretion of varnish can also be discovered. The diameter of tunnels on the cross profile is about ~1 μm (Fig. 2f).

3.3. Mineral assemblage of rock varnish

3.3.1. FTIR spectra analysis

Multiphases could be discriminated by the FTIR spectra of varnish sample, but they are dominated by clay minerals (Fig. 3), which is consistent with previous reports (Potter and Rossman, 1977). Four geomarkers including birnessite, quartz, clay minerals, and feldspar are identified. The main bands of birnessite are at 428, 468 and 513 cm^{-1}, which all arise from the Mn−O stretching vibration mode (Potter and Rossman, 1979b). The broad bands at 1625 and 3420 cm^{-1} result from

H−O−H bending and −OH stretching vibration modes of interlayer water molecules in birnessite or clays, respectively. The main bands of quartz are at 694, 779, 796 and 1088 cm^{-1}, which are attributed to the Si−O stretching vibration mode (Chukanov, 2014). The dominant band at 1038 cm^{-1} is attributed to the Si−O−Si stretching vibration mode of clay minerals (Potter and Rossman, 1977; Djomgoue and Njopwouo, 2013). Feldspar, whose main bands are overlapped by the bands of quartz and clay minerals, can be identified by its secondary bands at 588 (O−Si−O stretching vibration), 648 (O−Si−O stretching vibration) and 727 cm^{-1} (Si−Al(Si) stretching vibration) (Chukanov, 2014).

3.3.2. Micro-Raman spectra analysis

Minerals including birnessite, hematite, goethite, anatase, rutile and quartz can be identified in our measurement. Signals of clay minerals are not detected due to their poor sensitivity to Raman test. Birnessite can be identified by three major bands at 515, 590 and 627 cm^{-1}, and three secondary bands at 163, 295 and 396 cm^{-1} (Fig. 4a). According to the literatures, the major Raman bands of Mn oxides in 500–700 cm^{-1} have close relationship with their microstructures (Julien et al., 2003, 2004). For birnessite, the Raman band at 590 cm^{-1} is the fingerprint of Mn−O stretching vibration along the chains in MnO$_6$ octahedron; while the Raman band at 627 cm^{-1} corresponds to the Mn−O stretching vibration vertical to the chains in MnO$_6$ octahedron (Julien et al., 2003). The main Raman bands of hematite locate at 223 (A$_{1g}$, Fe−O sym str), 292 (E$_g$, Fe−O sym bend), 407 (E$_g$, Fe−O sym str), 475 (A$_{1g}$, Fe−O sym str) and 607 cm^{-1} (E$_g$, Fe−O sym bend) (Fig. 4b) (Faria et al., 1997; Legodi and Waal, 2007). Raman bands of goethite mainly occur at 243 (E$_g$), 299 (E$_g$, Fe−OH sym bend), 397 (E$_g$, Fe−O−Fe/−OH sym str), 478 (A$_{1g}$, Fe−OH asym str) and 552 cm^{-1} (Fe−OH asym str) (Fig. 4c) (Faria et al., 1997; Legodi and Waal, 2007). Anatase and rutile are the homogenous polymorphism of TiO$_2$ but display totally different Raman spectra. Anatase has a major band at 143 cm^{-1} (E$_g$) with three secondary Raman bands at 397 (B$_{1g}$), 513 (A$_{1g}$) and 637 cm^{-1} (E$_g$) (Fig. 4d) (Ohsaka et al., 1978), while the Raman bands of rutile occur at 145 (B$_{1g}$), 237 (crystal disorder induced), 447 (E$_g$) and 610 cm^{-1} (A$_{1g}$) (Fig. 4e) (Frank et al., 2012). Silicate minerals like quartz are common weathering products and
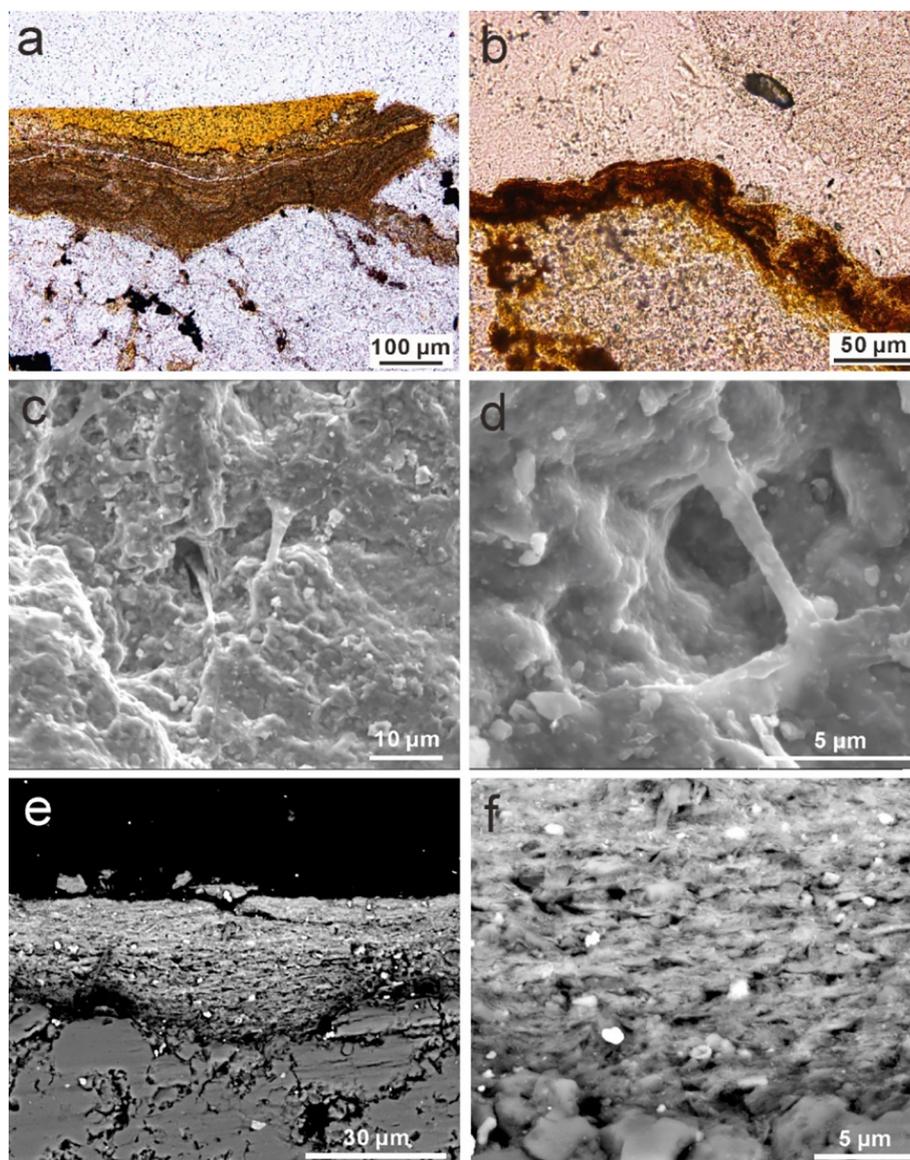
Fig. 2. Morphology of rock varnish under OP (a–b) and SEM (c–f). (a) (b) Layered varnish with alternating microlaminations. (c) (d) Secondary electron images demonstrating cave structures on the varnish surface. (e) (f) Back-scattered images showing fine mineral grains and small tunnels on the sample cross profile. Fig. 2b is revised from our previous work Lu et al. (2019).

quartz has two Raman bands at 208 and 466 cm^{-1} (A$_1$, Si—O sym str) (Fig. 4f) (Hemley, 1987).

3.3.3. TEM analysis

Under TEM, the elements mapping was first conducted to locate the region of elements in interest. The EDS data indicate a Mn-rich area with Mn content of 22.03% (Fig. 5a & b), and in this area a lattice photograph showing clear crystalline domains is picked out for further analysis (Fig. 5c). A region of the lattice photograph is indexed after fast Fourier transform (FFT), inverse FFT and calibration (Fig. 5d). The interplanar spacing *d* value of 0.72 nm can be assigned to the crystal faces of (001) of birnessite, which is diagnostic of the interlayer distance of adjacent MnO$_6$ octahedron sheets. The diffraction pattern shows a clear hexagonal lattice, consistent with the literatures that Mn oxides in rock varnish are mainly hexagonal birnessite (Krinsley, 1998). Similarly, two Fe-rich areas with Fe content of 78.46% and 39.39% are observed (Fig. 6a, b, e & f). The former one may be pure Fe oxides crystal with columnar morphology (Fig. 6a). A region displaying clear lattice fringes is selected (Fig. 6c), in which the interplanar spacing *d* values of 0.25 and 0.27 nm are most obvious (Fig. 6c & d) and can be

attributed to the lattice faces of (110) and (104) of hematite, respectively. The parallel lattice fringes in Fig. 6g display broad interplanar spacing *d* value of 0.5 nm, which can be assigned to the crystal faces of (020) of goethite (Fig. 6h). A Ti-rich area with Ti content of 28.77% is also observed, displaying granular morphology (Fig. 7a & b). Lattice fringes in Fig. 7c reveal *d* spacing values of 0.35 and 0.23 nm (Fig. 7d), which are attributed to the crystal faces of (101) and (004) of anatase, respectively.

3.4. Chemical composition and elements distribution patterns of rock varnish

3.4.1. Major elements revealed by EPMA

The electron microprobe results show the dominant elements in rock varnish are Si, Al, Mn and Fe, and the elements content demonstrates great fluctuations (Table 3). The content of MnO and FeO ranges from 8.66% to 29.20% and 6.95% to 15.33%, respectively, which is consistent with previous literatures that Mn/Fe oxides occupied one fifth to one third of the rock varnish (Dorn, 2007). Linear fitting of various elements against Mn in their oxides forms was carried out based
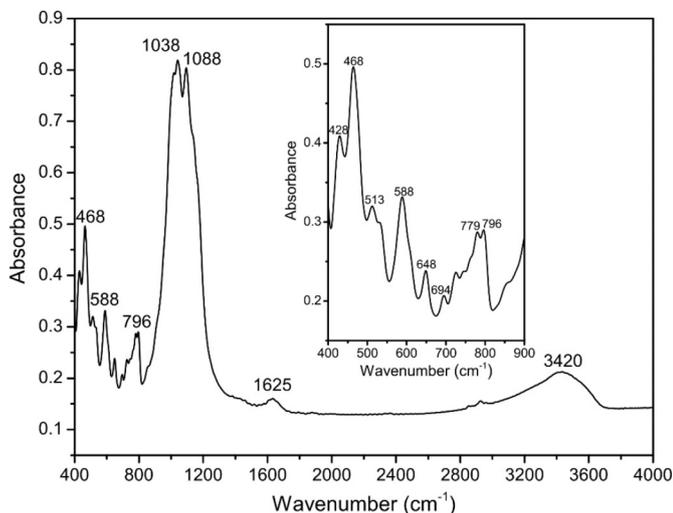
Fig. 3. FTIR spectra of rock varnish powders. The signals in the range of 400–900 cm^{-1} are magnified in the inserted rectangular region.

on the data in Table 3, and the results indicate that Si and Al display negative correlation with Mn (Fig. 8a & b). This phenomenon matches the macro alternating dark and light layers in thin sections, i.e., dark layers are rich in birnessite while light layers are rich in clay minerals (Perry and Adams, 1978; Liu and Broecker, 2008). However, Fe shows no correlation with Mn and the spots in Fig. 8c are randomly distributed. The positive correlation of Ba and Mn is most obvious (Fig. 8d). It may suggest the strong affinity of Ba to Mn oxides probably due to the ion exchange.

3.4.2. Trace elements revealed by LA-ICP-MS

The chemical composition of rock varnish samples was compared with that of soil dust which was considered to be the major material source of varnish to study the elements enrichment factor (Table 4). The spidergram indicates that elements in rock varnish can be divided into four groups (Fig. 9): 1) elements including Mn, Ba and Pb are greatly enriched in varnish to ~50–150 times; 2) elements including Co, Ni, Rb, Y, rare earth elements (REEs), W, Th and U are slightly enriched in varnish with a factor of ~2–10. Additionally, the enrichment of light REEs is more significant than heavier REEs and a positive anomaly of Ce is obtained (Fig. 10); 3) elements including Si, Al, Fe, Mg, Na, P, Sc, Ti, Cr, Sr, Zr, Nb, Hf and Ta are not enriched in varnish and the enrichment factor ranges from ~0.5 to 2; 4) elements Ca and Cs are depleted in rock varnish with a factor of ~0.2–0.1.

3.4.3. Elements distribution patterns

Under SEM, the EDS mapping indicates that within the profile of thin section, the Mn content demonstrates great fluctuations: Mn-rich and Mn-poor bands can be discriminated in varnish with thickness of 20 μm, and each band is ~2–4 μm in width (Fig. 11b). Fe is evenly distributed throughout the cross profile (Fig. 11c). Si, a common petrogenetic element, is not enriched in varnish when compared with its high content in substrate (Fig. 11d). Si-rich mineral clasts (e.g., quartz particles) can be identified in varnish. These observations are coincident with the macro color variation of varnish laminations (Fig. 2a & b) and linear fitting results of element content (Fig. 8).

On nanometer-scale, the compositional maps based on STEM EDS imaging clearly show the close intergrowth relationship of Mn, Fe and Ti in varnish FIB ultra-thin section (Fig. 12c). The Mn-rich matrix almost prevails over the whole 2-D plane area (Fig. 12d). The mixtures of Fe-rich minerals are surrounded by Mn-rich minerals. Some Fe-rich
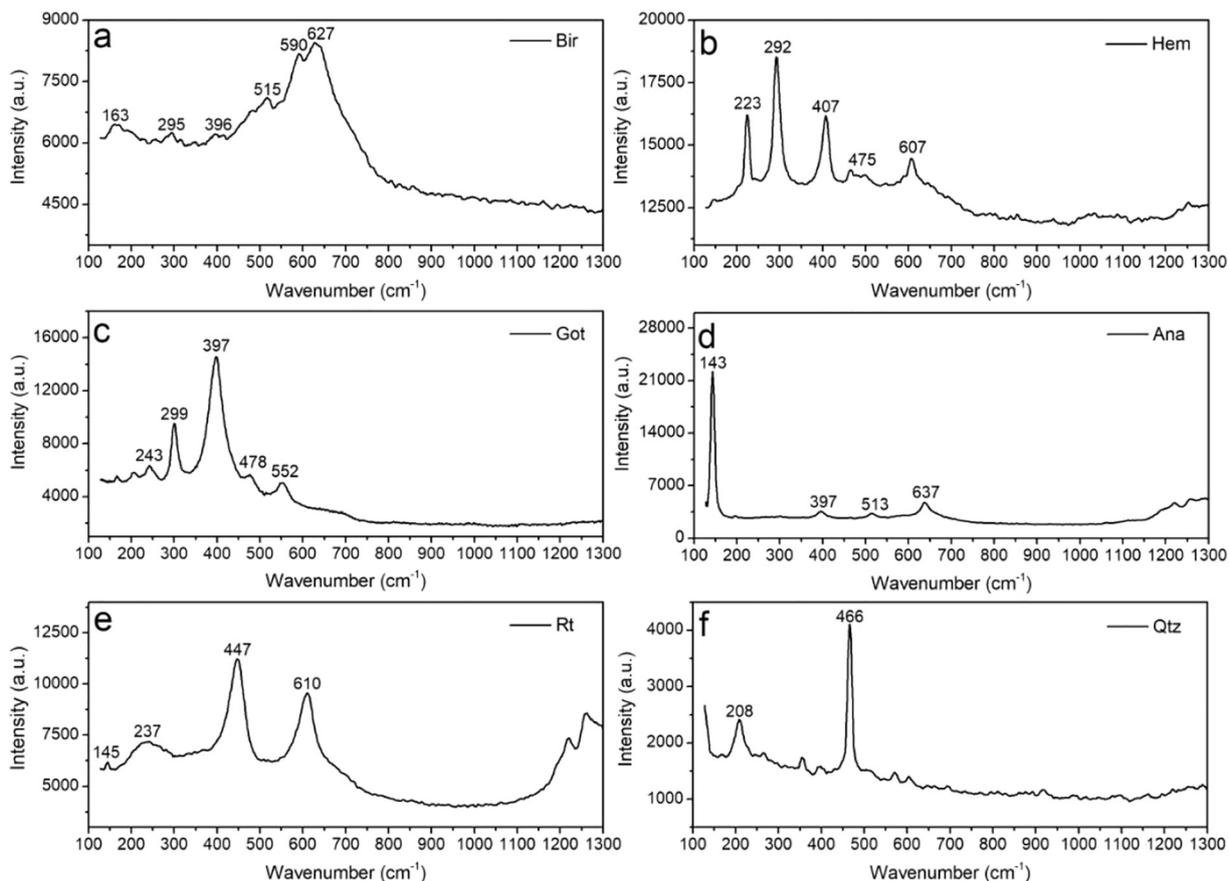

Fig. 4. Micro-Raman spectra of rock varnish thin sections. (a) Birnessite (Bir); (b) hematite (Hem); (c) goethite (Gt); (d) anatase (Ant); (e) rutile (Rt); (f) quartz (Qtz).
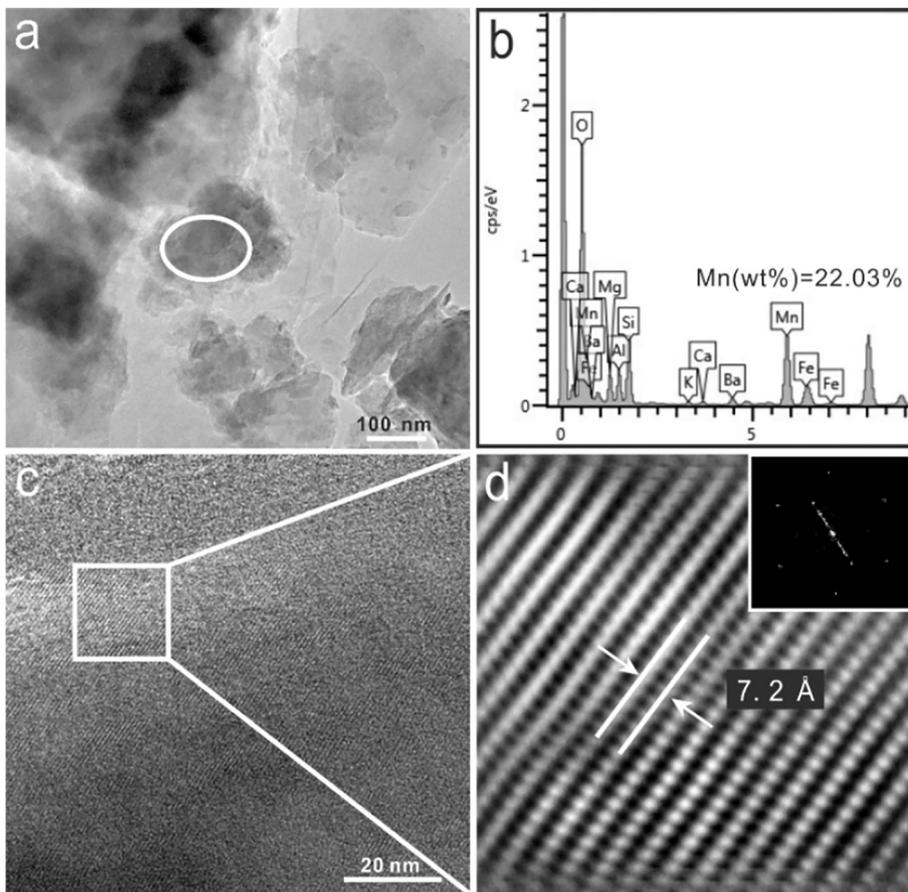
Fig. 5. TEM morphology (a), EDS data (b), lattice photograph (c, d) and diffraction pattern (d) of Mn-rich grains. Panel b shows the chemical composition of the selected oval area in panel a. Lattice fringes and diffraction pattern in panel d are the FFT and inverse FFT results of selected rectangular area in panel c. The *d* value of the one-dimensional lattices is 0.72 nm (d) and can be attributed to the crystal faces of (001) of birnessite.
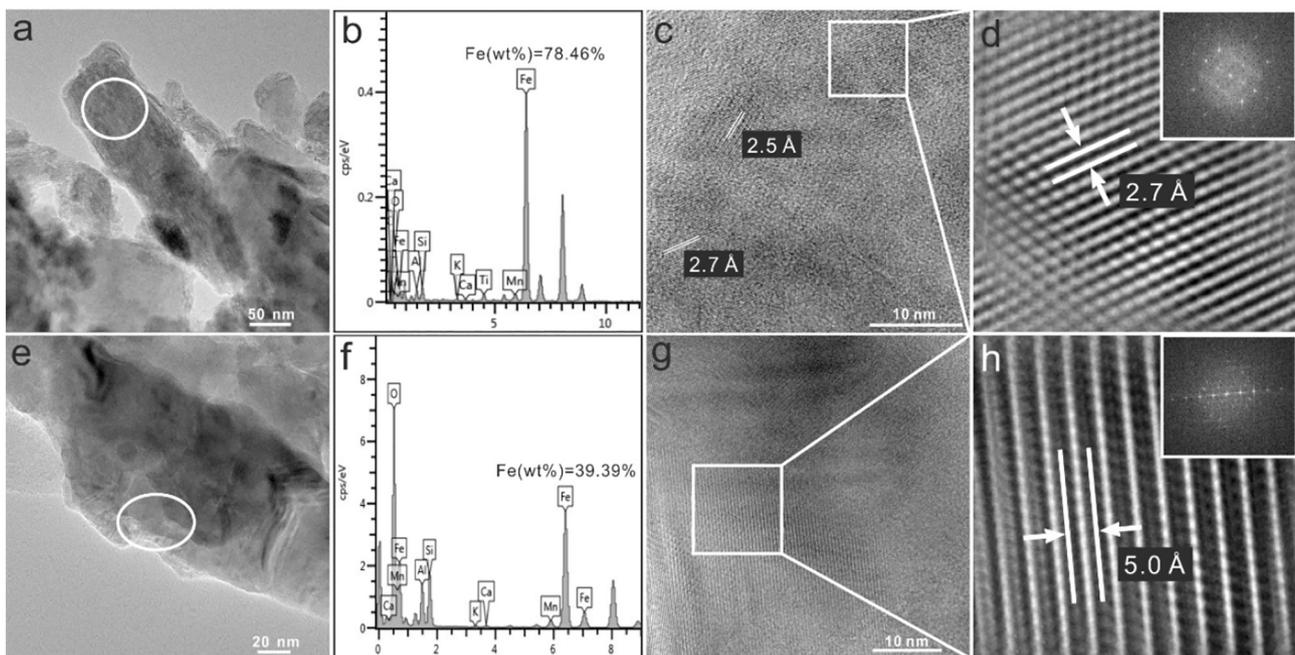

Fig. 6. TEM morphology (a, e), EDS data (b, f), lattice photograph (c, d, g, h) and diffraction pattern (d, h) of Fe-rich grains. Panels b and f show the chemical composition of the selected oval areas in panels a and e, respectively. Lattice fringes and diffraction pattern in panels d and h are the FFT and inverse FFT results of selected rectangular areas in panels c and g, respectively. The *d* values of the two-dimensional lattices are 0.25 and 0.27 nm (c, d) and can be attributed to the crystal faces of (110) and (104) of hematite. The broad interplanar spacing *d* value of 0.5 nm in panels g and h can be assigned to the crystal faces of (020) of goethite.
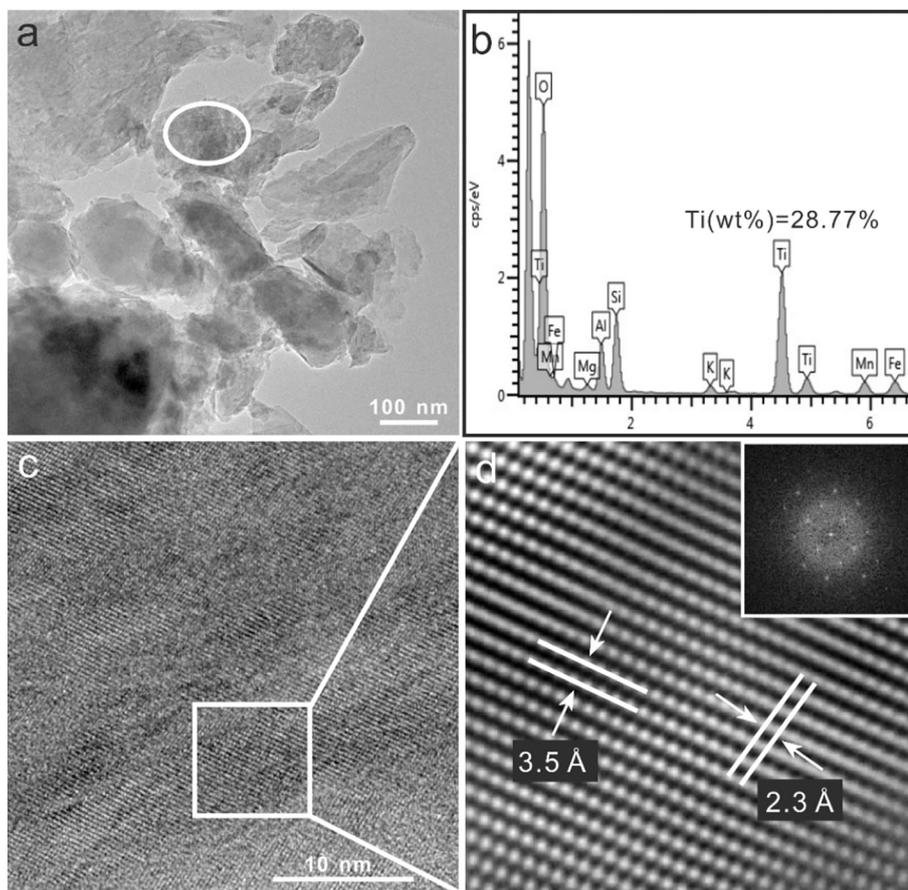
Fig. 7. TEM morphology (a), EDS data (b), lattice photograph (c, d) and diffraction pattern (d) of Ti-rich grains. Panel b shows the chemical composition of the selected oval area in panel a. Lattice fringes and diffraction pattern in panel d are the FFT and inverse FFT results of selected rectangular area in panel c. The d values of the two-dimensional lattices are 0.35 nm and 0.23 nm (d), and can be attributed to the crystal faces of (101) and (004) of anatase.

patches with size of ~100 nm are resolvable (Fig. 12e). Ti-rich mineral clasts with size of 50–100 nm are common in the section (Fig. 12f), which are also wrapped by Mn-rich materials.

3.5. EPR signals of rock varnish

Fe(III) and Mn(IV) are the main contributors to EPR signals of rock varnish, because only elements with unpaired electrons in magnetic field can produce electron spin resonance signals. Fe(III) yields peak at ~1500 G and Mn(IV) yields peak at ~3300 G. These signals are characterized by broad linewidth, which is an important parameter to identify the origin of these minerals (Kim et al., 2011). Specifically, the linewidth of Mn(IV) peak of GD-1, GD-2, GD-3, GD-4 and GD-5 sample is 908, 776, 890, 764 and 892 G, respectively (Fig. 13).

Table 3
EPMA data of rock varnish thin sections.

Spot	Na$_2$O	K$_2$O	TiO$_2$	MgO	SiO$_2$	MnO	Al$_2$O$_3$	P$_2$O$_5$	FeO	Cl	CaO	BaO	Total
1	0.18	1.00	0.28	2.75	31.51	19.24	18.61	1.61	11.85	0.21	1.80	1.64	90.68
2	0.48	2.82	0.42	3.16	29.17	14.14	17.23	1.23	11.56	0.22	1.68	1.32	83.42
3	0.47	2.81	0.41	2.40	27.26	13.49	16.86	1.18	10.69	0.28	2.03	1.17	79.04
4	0.47	1.99	0.31	3.14	17.88	29.20	12.34	0.54	7.25	0.12	1.63	4.27	79.13
5	0.39	3.14	1.09	3.35	35.14	9.39	20.53	0.88	9.61	0.10	1.16	0.85	85.64
6	0.47	3.64	1.09	2.82	34.16	11.01	19.04	0.93	9.39	0.16	1.07	0.84	84.61
7	0.44	2.51	0.57	2.16	33.87	10.98	20.73	1.10	7.97	0.23	1.59	1.32	83.47
8	0.47	2.89	1.13	3.79	31.93	10.23	18.77	1.18	11.03	0.18	1.69	0.90	84.19
9	0.43	2.99	0.31	5.05	31.65	10.35	18.27	0.77	10.49	0.15	1.13	1.04	82.61
10	0.27	1.87	0.51	1.98	36.74	12.01	19.10	1.01	7.00	0.29	1.31	1.22	83.31
11	0.60	2.89	0.41	4.01	29.93	13.32	18.33	0.89	9.01	0.21	1.17	1.50	82.26
12	0.53	2.77	0.69	3.99	28.20	11.72	15.61	0.93	15.33	0.29	1.22	1.23	82.51
13	0.28	2.21	0.66	2.60	29.24	12.90	17.41	0.92	11.26	0.13	1.48	1.44	80.52
14	0.07	0.33	77.15	0.58	4.44	1.10	2.97	0.19	3.68	0.08	0.35	0.76	91.70
15	0.49	3.86	0.38	3.11	34.62	8.66	20.29	0.85	9.32	0.23	1.24	0.75	83.79
16	1.04	2.54	0.24	2.44	39.61	8.81	17.14	0.71	8.94	0.13	1.47	0.84	83.91
17	0.45	2.70	5.37	3.49	30.82	8.88	16.27	0.82	10.14	0.30	1.16	0.75	81.14
18	0.57	2.48	0.35	2.49	23.94	16.02	14.35	1.01	6.95	0.46	1.75	1.73	72.11
19	0.45	2.77	0.44	3.48	31.57	11.03	16.52	2.26	10.62	0.22	3.45	1.02	83.82
20	0.20	1.55	1.09	3.37	34.33	9.60	21.30	1.10	9.63	0.12	1.27	0.84	84.39

Note Ti content in spot 14 is extremely high, indicating that the electron beam coincidentally hits a TiO$_2$ mineral clast. Thus, this spot is excluded in the figure of correlation curves (Fig. 8). The total content does not yield a value of 100% mainly because C is not included in this analysis. Organic matters are abundant in rock varnish which may occupy a ratio of ~10–15%.
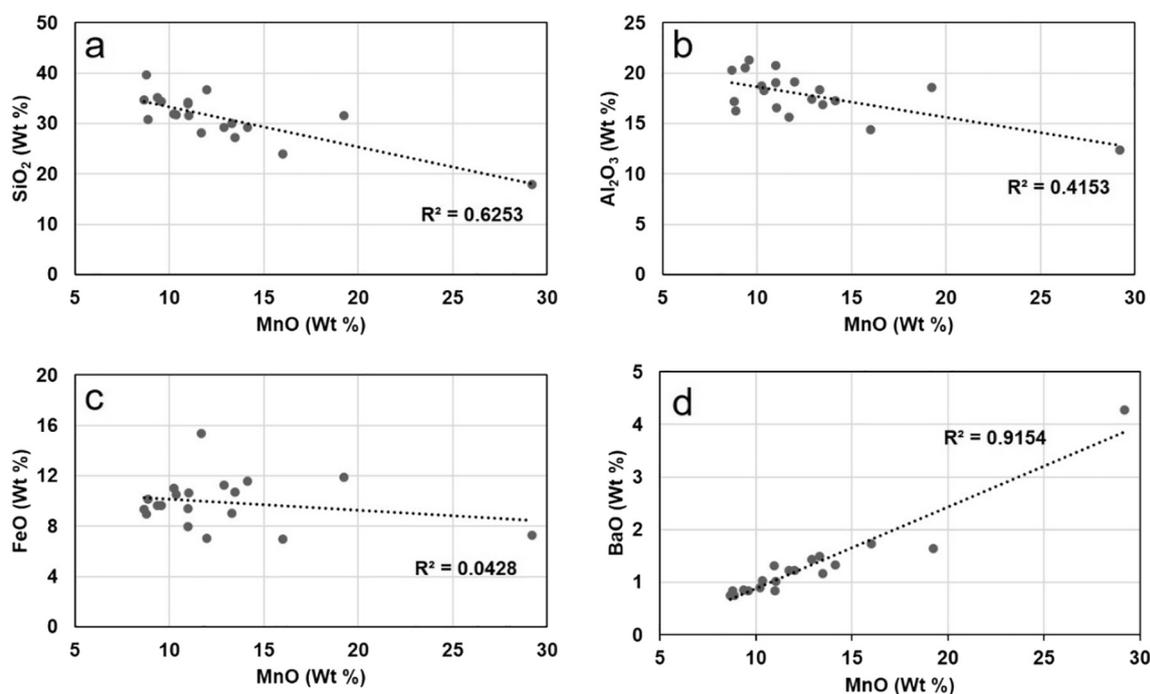
Fig. 8. Correlation curves of elements with Mn. Mn content shows a negative correlation with Si (a) and Al (b) and a positive correlation with Ba (d). Fe content does not change as a function of Mn (c).

To identify the ROSs generated by varnish suspension, EPR test was conducted before and after illumination. The EPR spectra were dominated by the signals of soluble Mn(II) species. Six hyperfine splittings of Mn(II) can be identified from 3200 to 3800 G, while signals of ROSs mainly occur in the range of 3450–3550 G (Fig. 14c). Before illumination, three diagnostic peaks of singlet oxygen ($^1O_2$) can be identified (Fig. 14a). After illumination, four diagnostic peaks of hydroxyl radical (OH·) can be identified (Fig. 14b). Hydroxyl radical is a strong oxidant that is mainly formed from hydroxyl (OH$^-$) through photocatalysis by semiconducting minerals in varnish suspension.

3.6. Laboratory simulation of abiotic photo-oxidation of Mn(II) by semiconducting minerals

Above researches indicate rock varnish is rich in metal oxide minerals including goethite, hematite, rutile and anatase which are all responsive to solar light irradiation, and varnish suspension can generate ROSs under illumination. Therefore, laboratory experiments were conducted using these metal oxide minerals to check if they can promote Mn(II) oxidation through photocatalysis. Here we just assume all photo-oxidation products are Mn(IV) in order to make comparison for the oxidation rates easily. And the tiny amount of Mn oxidation products prevents us from conducting any further characterization. During reaction, the contents of Mn(IV) increase in all systems as a function of time (Fig. 15; Table 5). However, far fewer products are produced in blank groups with a rate of 0.31 μM_{Mn} h^{-1}, indicating that oxidation of Mn(II) by O_2 is very slow. The presence of goethite and hematite can enhance Mn(II) oxidation rates to 2.45 and 0.51 μM_{Mn} h^{-1} in dark system (Fig. 15a & b), respectively, although rutile and anatase do not demonstrate similar trend (Fig. 15c & d). This is mainly due to the strong surface catalysis effect of goethite and hematite nano-particles (X. Wang et al., 2015; Y. Wang et al., 2015; Lan et al., 2017). When light illumination is introduced in the system, the oxidation rates of Mn (II) are greatly enhanced. After reaction of 8 h, the average oxidation rates of Mn(II) reach 2.47, 1.14, 2.26 and 0.65 μM_{Mn} h^{-1} in goethite, hematite, rutile and anatase group, respectively (Table 5). The oxidation speeds gradually decrease with time and keep stable after 8 h

because of the decrease of pH condition in the system. All the metal oxide minerals in our experiments are responsive to solar light irradiation, and they can promote Mn(II) oxidation through photo-generated holes or ROSs like OH· (Fig. 14). In this work, the oxidation of Mn (II) can be promoted by 2.10–7.97 times through photocatalysis when compared with homogenous solution oxidation.

4. Discussion

4.1. Evidence for the aqueous genesis and abiotic origin of rock varnish

Elements including Mn, Ba and Pb are greatly enriched in rock varnish and the dominant mineral phase of Mn oxides is birnessite. Similar enrichment factors indicate that these elements can be incorporated into a common mineral phase, i.e., large ions such as Ba and Pb can occupy interlayer sites of birnessite to balance the negative charge of MnO_6 octahedron sheets. Elements including Co, Ni, Rb, Y, REEs, W, Th and U are slightly enriched in varnish with a factor of ~2–10. These elements are particle-reactive and their enrichment is attributed to the good solubility of leaching from clay minerals and adsorption by Mn oxides (Thiagarajan and Lee, 2004; Goldsmith et al., 2014). The most obvious feature in REEs enrichment is the positive anomaly of Ce (Fig. 10). Commonly Ce cannot be easily fractionated from La, however, in aqueous system with more oxidizing conditions, a large fraction of Ce is in +4 states, which differs from the dominant +3 valence states of the neighboring REEs. Thus, Ce has a higher ionic potential and can be adsorbed by Mn/Fe oxides more easily (Liu et al., 1998; Alibo and Nozaki, 1999). The high field strength elements (Zr, Nb, Hf and Ta) are also particle-reactive in solution but are not enriched in varnish at all. This can be explained by their insolubility compared with other trace elements, i.e., they are difficult to leach from soil dust. Other non-enriched elements include Si, Al, Fe, Mg, Na, P, Sc, Ti, Cr and Sr which comprise more than half of the varnish material. These elements can be regarded as passive incorporation in varnish formation. The enrichment of Mn in varnish by ~100 times suggests that most part of soil dust is not incorporated into varnish. This unconsolidated part is physically removed after leaching and precipitation of Mn. Ca and Cs

Table 4
ICP-MS data of rock varnish powders and soil dust.

| Sample name	GD-1	Dust-1	GD-2	Dust-2	GD-3	Dust-3	GD-4	Dust-4	GD-5	Dust-5
Major elements (wt%)										
SiO₂	50.33	53.65	49.58	54.35	46.08	54.48	60.40	63.23	48.32	59.80
Al₂O₃	18.70	12.35	16.50	12.90	16.30	11.97	20.07	13.89	13.07	12.74
CaO	1.70	8.05	1.29	8.51	3.05	8.13	1.91	4.63	2.65	6.92
Fe₂O₃	9.30	5.52	16.18	5.71	6.61	5.03	8.21	6.79	9.62	5.20
MgO	1.52	3.26	2.63	3.19	2.13	2.91	3.75	2.41	5.30	2.63
Na₂O	3.10	4.01	3.70	2.32	2.49	2.91	2.65	3.19	1.07	2.83
Trace elements (ppm)										
P	738.79	820.50	382.88	630.00	907.69	552.10	454.67	783.20	980.33	810.20
Sc	22.33	13.82	9.81	13.78	39.09	12.58	25.12	17.72	36.62	13.41
Ti	3875.07	4533.95	5240.63	4457.24	10,869.59	4499.67	7814.00	7865.00	3422.24	4693.30
Cr	42.67	82.62	129.62	91.06	88.02	78.84	227.68	94.71	41.12	74.42
Mn	97,327.38	805.88	109,187.50	861.95	92,211.10	806.78	76,489.50	1031.56	36,402.64	854.68
Co	218.43	16.09	124.48	16.35	69.79	14.32	77.16	15.31	31.76	13.50
Ni	90.97	47.88	82.69	50.88	237.92	46.56	115.35	32.77	110.27	41.39
Rb	179.32	80.48	151.89	89.06	70.45	81.90	99.18	73.40	113.08	90.91
Sr	365.20	245.98	223.02	266.33	301.33	577.60	278.15	265.58	264.41	238.25
Y	72.36	38.07	131.64	31.35	67.38	31.74	122.70	54.35	80.44	40.29
Zr	166.57	224.64	201.84	177.05	225.11	281.92	486.00	446.68	282.90	320.63
Nb	23.45	12.43	10.43	12.29	18.76	12.29	18.60	14.97	12.13	15.46
Cs	1.84	6.36	1.31	7.12	0.46	6.20	2.01	4.57	1.29	6.20
Ba	7445.81	346.16	13,790.03	430.95	21,316.38	450.23	23,252.01	403.40	10,290.63	498.76
La	244.08	30.57	134.44	30.64	78.76	31.06	169.56	34.90	110.62	37.68
Ce	602.90	60.42	304.55	60.80	670.24	62.07	1119.38	92.66	326.54	73.75
Pr	38.10	7.30	24.13	7.14	29.06	7.34	50.22	11.10	31.77	8.74
Nd	137.28	31.33	80.25	31.76	65.98	32.58	135.80	46.61	115.96	37.65
Sm	25.42	6.30	17.00	6.16	21.35	6.28	27.14	8.98	21.34	7.30
Eu	4.85	1.50	3.08	1.42	2.91	1.42	4.70	1.79	4.25	1.58
Gd	20.74	5.97	16.82	5.43	11.03	5.59	16.46	8.14	21.57	6.58
Tb	3.38	1.02	3.34	0.90	1.86	0.88	3.10	1.39	3.19	1.14
Dy	18.74	6.21	19.13	5.27	12.00	5.46	17.73	8.93	14.37	6.75
Ho	3.52	1.31	3.45	1.08	2.68	1.13	3.84	1.87	2.96	1.46
Er	8.77	3.86	8.90	3.24	7.50	3.22	15.38	5.48	9.06	4.13
Tm	1.27	0.54	1.54	0.43	1.16	0.49	1.75	0.82	1.15	0.61
Yb	8.61	3.43	7.86	2.64	8.20	2.98	15.02	5.22	11.20	3.82
Lu	1.23	0.60	1.15	0.45	1.15	0.50	1.56	0.92	1.20	0.65
Hf	7.06	6.06	5.31	5.20	6.86	8.08	12.01	11.65	12.08	9.03
Ta	1.43	1.09	0.72	1.24	1.14	1.16	1.02	1.39	1.03	1.51
W	4.09	1.61	1.78	1.59	2.71	1.67	1.99	1.48	1.61	1.89
Pb	3044.96	17.22	1751.70	16.04	485.63	15.10	1706.22	19.57	810.40	20.02
Th	25.01	9.73	31.38	10.40	19.14	9.28	32.96	18.06	36.44	13.22
U	12.54	2.75	10.91	2.69	12.94	2.99	10.90	3.25	12.69	2.98
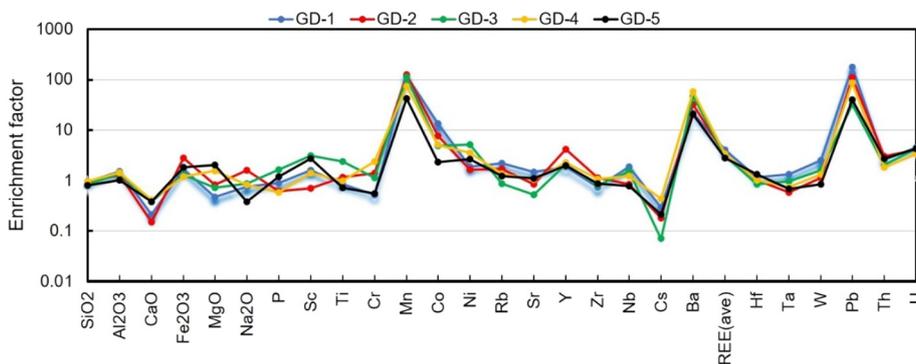
Fig. 9. Spidergram showing elements enrichment degree in rock varnish compared with soil dust. The enrichment factor of REEs is given as an average value.

are largely depleted in respect to local dust due to their high solubility in natural waters. Once in solution, Ca and Cs become mobile, and their high solubility prevents them from being precipitated with Mn/Fe oxides and allows them easily leach from any detrital components remaining in varnish. Therefore, the above elements abundance patterns in rock varnish indicate its formation begins in aqueous system.

The key process of varnish formation is the oxidation of soluble Mn (II) to form insoluble species. Opinions about this process remain highly controversial including both biotic and abiotic hypotheses. In abiotic

literatures, the slight fluctuation of pH condition is the key factor controlling the release of Mn(II) and accumulation of Mn oxides. Rainfall and dew with pH of ~5.7 and Eh of ~0.8 trigger the release of Mn(II) from soil dust (Thiagarajan and Lee, 2004). At this condition, Mn (II) is more soluble and mobile while Fe(II) remains in the immobile form of Fe(OH)₃. Thus, dissolved Mn content is enhanced relative to the dissolved Fe content. Precipitation of Mn(II) on rock surface needs this cation to be oxidized to form insoluble species. The chemical condition of semiarid or arid regions is slightly alkaline with pH value of 7.2–8.4
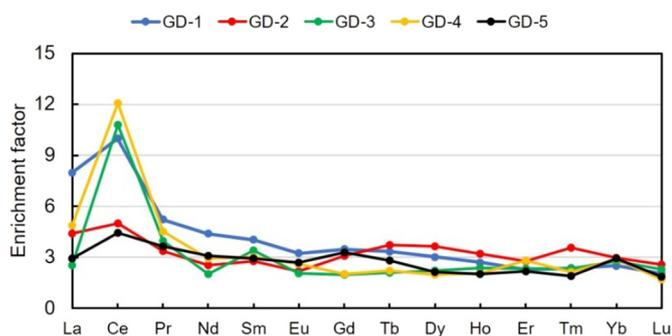
Fig. 10. Abundance of REEs in rock varnish normalized to soil dust.

and Eh value of 0.4–0.7 after water evaporation (Goldsmith et al., 2014), in which condition the stable Mn species are Mn(II) or Mn(IV) O_2. This phenomenon confirms that abiotic oxidation of Mn(II) in slightly alkaline arid regions is feasible. The pH fluctuation also contributes to the formation of varnish microlaminations which are proved to have important palaeoenvironmental implications: Mn-rich dark layers were formed during wetter periods while Si/Al-rich light layers were formed during drier periods (Krinsley et al., 1995; Broecker and Liu, 2001). Supporters of biotic formation mechanism argued that this was attributed to the fact that wetter and less alkaline conditions were more favorable for the growth of the Mn-enhancing bacteria (Krinsley, 1998; Dorn, 2007). However, some researchers proposed that the laminations were only results of a competition between the accumulation rate of Mn and the adhesion rate of clay minerals (Goldsmith et al., 2014). Wetter periods lead to higher dust mobilization and more released Mn(II), while during drier periods Mn would be dispersed in the large amount of clay minerals.

The origin of Mn oxides minerals can be identified by their totally different EPR spectral signatures (Kim et al., 2011). A narrower linewidth (< 560 G) can be observed for bio-Mn oxides than for synthetic Mn oxides (> 1200 G). The narrower linewidth of bio-Mn oxides is attributed to the high amounts of layer site vacancies (15–50%), fine particle size, and absence or lack of Mn(III) in bio-Mn oxides (Kim et al., 2011). Subsequent researchers used this method to see which category the Mn oxides in rock varnish belong to, and they observed an

intermediate linewidth between 600 and 1200 for their samples (Kim et al., 2011; Macholdt et al., 2017). In our results, the diagnostic peak related to Mn oxides appears at ~3300 G and the samples fall into the category of linewidth of 764–908 G. According to above literatures, abiotic process should be involved in the formation of Mn oxides in rock varnish.

4.2. Geological conditions for photo-oxidation of Mn(II) in rock varnish

Field investigation indicates that Mn-rich varnish covers the upper surface of pebbles which are exposed to the solar light and atmosphere, while Fe-rich stains grow on the bottom side of rocks. Distinct color border can be discriminated on the pebble rim. Additionally, varnish also develops on the topmost part of rock crack, an area which can be irradiated obliquely by the solar light. All these observations suggest the occurrence of rock varnish is closely related with solar light. Caves on varnish surface and tunnels within varnish thin sections are abundant, which can promote the absorption of solar light and intrusion of rain drops.

Besides clay minerals, rock varnish consists of birnessite, hematite, goethite, anatase and rutile. These transition metal oxides are the major components of rock varnish and occupy a weight percentage of 8.66%–29.20% (MnO), 6.95%–15.33% (FeO) and 0.24%–5.37% (TiO$_2$), respectively (Table 3). These metal oxide minerals are well-known semiconducting materials responsive to solar light. The solar light, which has been illuminating the rock surface for billions of years, is likely to have played some roles during the formation of varnish. The band gap of metal oxide minerals in varnish ranges from 1.82 to 3.2 eV (Table 6). Thus, the required maximum excitation wavelength for photocatalysis is 401–683 nm, which is well within the wavelength range of visible light. Under solar light illumination, excited electrons can jump from the valence band (VB) of metal oxide minerals to the conduction band (CB), thus leaving photo-generated holes in the VB. Holes in VB can oxidize Mn(II) to Mn(III/IV) to form insoluble species while electrons in CB can reduce O_2 in the environment (Fig. 16). Our laboratory experiments have also confirmed the feasibility of photo-oxidation of Mn(II) catalyzed by metal oxide minerals.

In literatures, even pre-formed birnessite can promote oxidation of Mn(II). Learman et al. (2011) indicated that Mn(II) oxidation by birnessite can be accelerated in presence of both organics and light,
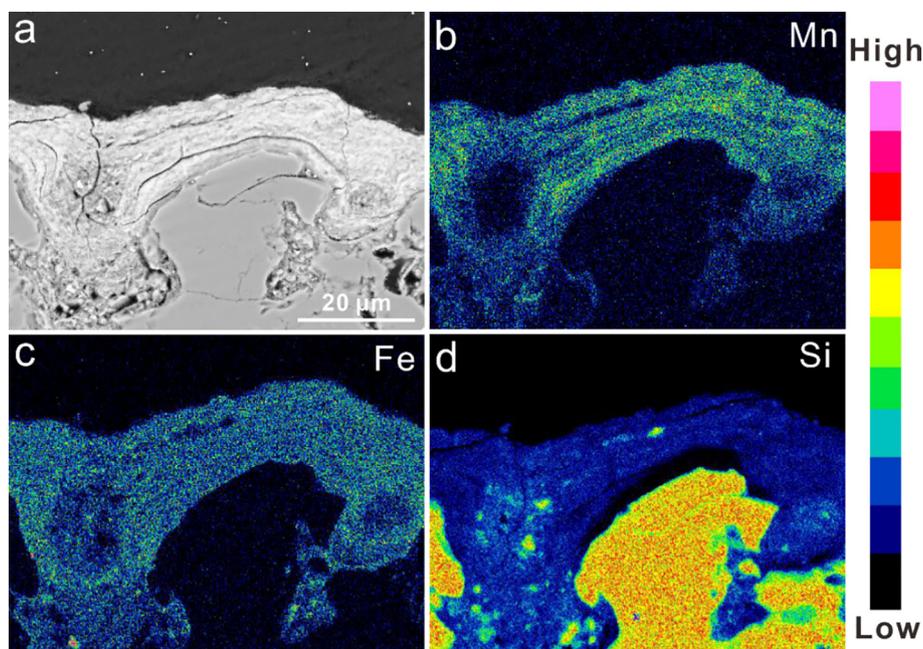

Fig. 11. EDS mapping of elements within varnish thin section under SEM. This figure is revised from our previous work Lu et al. (2019).
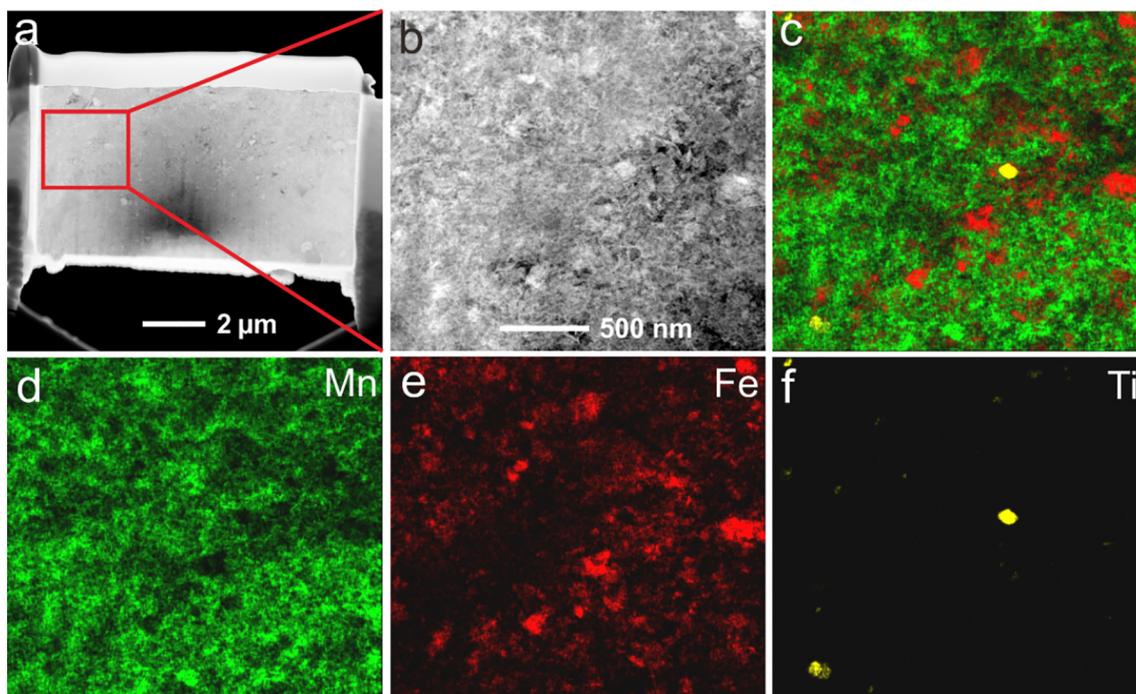
Fig. 12. Element distribution maps obtained by STEM. Panels a and b are overview images. Panel c is an overlay of Mn (green), Fe (red) and Ti (yellow) distribution. Most of the black areas in this panel are rich in Si. Panels d, e and f are a Fe map, Mn map and Ti map, respectively. (For interpretation of the references to color in this figure legend, the reader is referred to the web version of this article.)
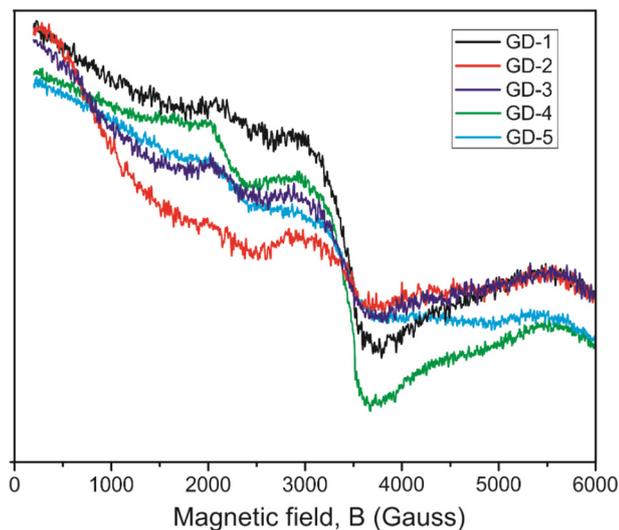

Fig. 13. EPR spectra of five rock varnish samples. Signals of Mn(IV) occur at ~3300 G.

implicating ROSs (e.g., $O_2^- \cdot$) in aiding abiotic oxidation. Georgiou et al. (2015) reported ROSs formed through photocatalysis of metal oxide minerals (mainly TiO_2 and Fe_2O_3) in arid regions. In aqueous system, the electron of hydroxyl (OH^-) in water can be captured by holes in VB to form hydroxyl radical ($OH\cdot$) with strong oxidizing capability (Xu et al., 2013), which can be used to oxidize Mn(II) to Mn (IV)O_2 (Fig. 16). And in laboratory, we have successfully detected EPR signals of $^1O_2$ and $OH\cdot$ through photocatalysis of varnish suspension (Fig. 14). Furthermore, the close intergrowth relationship of Mn/Fe/Ti-rich particles on nanometer scale revealed by FIB ultra-thin sections (Fig. 12) contributes to the formation of different types of semiconductor heterojunctions. The matched band structure favors the transfer of photo-generated electrons and holes (Fig. 16). For example, it is thermodynamically feasible that electrons transfer from the CB of

hematite to that of anatase, and holes transfer from the VB of anatase to that of hematite (Fig. 16). This space separation of photo-generated electrons and holes is beneficial to prevent charge recombination, thus resulting in higher photocatalytic activity (X. Wang et al., 2015; Y. Wang et al., 2015). Commonly the chemical composition of natural metal oxide minerals is deviated from the standard stoichiometry due to isomorphous substitution and lattice vacancy. In rock varnish, trace elements are scavenged by Mn/Fe oxides or oxyhydroxides to various degree. In the field of photocatalytic materials, dopants and vacancies are well-known to narrow the band gap and introduce intermediate impurity levels in the forbidden band of metal oxide minerals (e.g., Umebayashi et al., 2002; Velev et al., 2005; Kwon et al., 2009; Lucht and Mendozacortes, 2015), which can broaden the light responding wavelength range of catalysts. And more pairs of electrons and holes can be generated upon illumination because sunlight contains multiple wavelengths.

4.3. Kinetic considerations for photo-oxidation of Mn(II) in rock varnish

The key controversy of varnish genesis focuses on the oxidation mechanism of Mn. Typical varnish formed in warm deserts grows at rates of microns per millennium (Dorn, 1998; Liu and Broecker, 2000). However, almost all existing models generate rates of accretion far greater than those observed in nature, and a rate-limiting step is needed for each hypothesis (Dorn, 2007; Krinsley et al., 2017). The biotic model relies on a wide variety of organisms (Krumbein, 1968; Dorn and Oberlander, 1981; Krumbein and Jens, 1981; Billy and Blanc, 1982; Palmer et al., 1986; Eppard et al., 1996; Sterflinger et al., 1999; Northup et al., 2010) and organic matters such as amino acids (Perry et al., 2003; Perry and Kolb, 2004b), isotopes of carbon (Dorn and DeNiro, 1985), fatty acid methyl esters (Schelble et al., 2005) to oxidize Mn. If all of these organisms and organic matters assist in varnish formation, rates would be several orders of magnitude higher than empirical observation (Dorn, 2007; Krinsley et al., 2017). Proponents of biotic model use the rarity of direct in situ observations of bacteria enhancing Mn and Fe on varnish surfaces to solve the rate-limiting issue
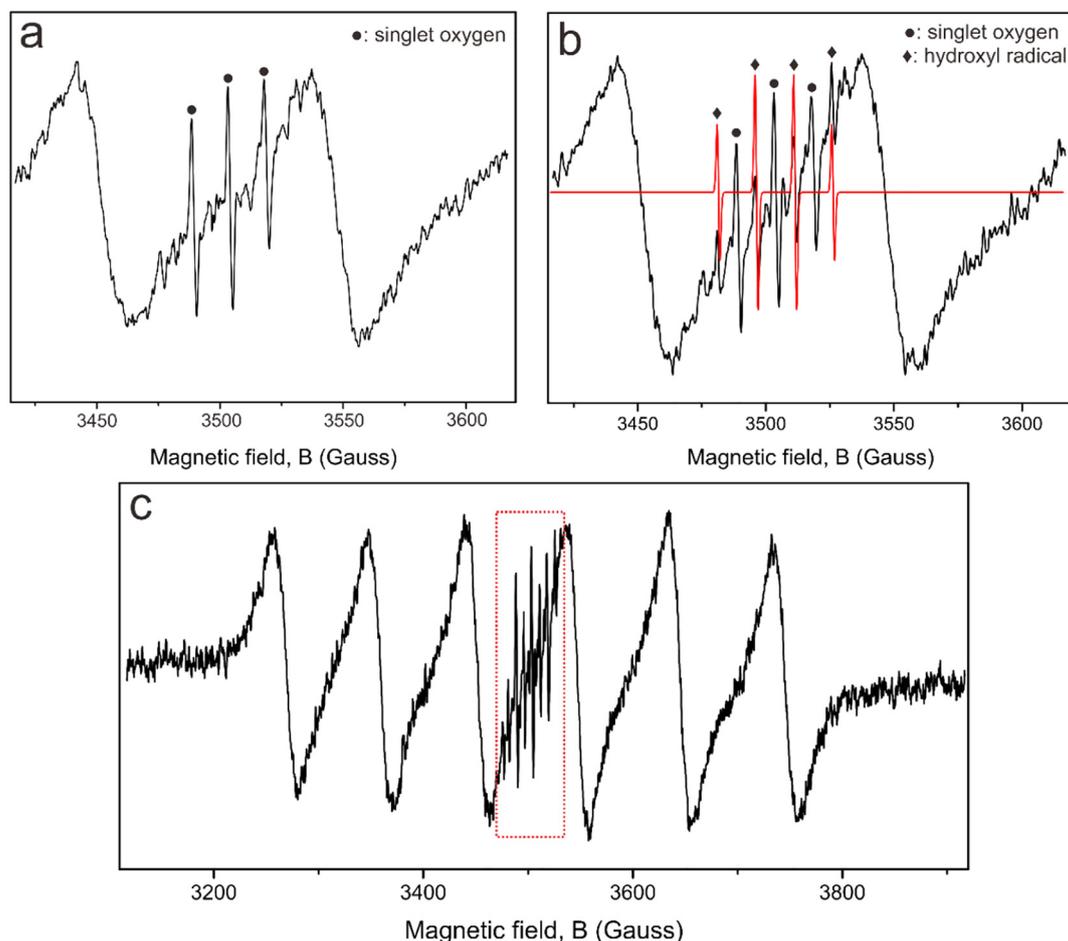
Fig. 14. EPR spectra of ROSs produced by varnish suspension before (a) and after illumination (b, c). Panel b is the magnified version of the red rectangle region in panel c. The red curve in panel b is the standard signals of hydroxyl radical. (For interpretation of the references to color in this figure legend, the reader is referred to the web version of this article.)

(Dorn and Krinsley, 2011; Krinsley et al., 2017), which indicates that only a very small portion of these organisms actually contribute to the formation of varnish. The abiotic hypothesis requires weak acid rainfall to leach Mn out of the dust, followed by reprecipitation through slight increase in pH as water evaporates (Engel and Sharp, 1958; Smith and Whalley, 1988; Thiagarajan and Lee, 2004; Goldsmith et al., 2014). Dorn (2007) calculated that known rates of dust deposition in warm desert and concentrations of Mn in this dust would generate varnish 100–10,000 times faster than the real rate. However, the real Mn^{2+} molarity on rock surface is only 10–30 μM (Goldsmith et al., 2014), three orders of magnitude less than that in the dust (~500 ppm). This phenomenon indicates that only a small portion of Mn is released from dust and contributes to the formation of varnish.

Considering the complexity of natural settings, multiple reactions may be involved in the formation of varnish and it is hard to tell which mechanism prevails over another. Our work indicates a new oxidation model, which may contribute to the formation of varnish but has been neglected by previous researchers for a long time. Goldsmith et al. (2014) estimated the real accumulation rates of Mn in varnish from Negev Desert and their method yielded a value of 320–680 ppm/year. Morgan (2005) calculated the kinetics for oxidation of Mn(II) in aqueous system. Using parameters similar to Mn molarity in micro-basin on rock surface, he calculated that amounts of Mn accumulation would be 35,000, 490 and 36 ppm/year via bacterial oxidation, metal oxide catalysts and homogenous solution oxidation, respectively (Morgan, 2005; Goldsmith et al., 2014). The real accumulation rate in varnish coincidently matches the theoretical oxidation rate via metal oxide

catalysts. The Mn accumulation rate by bacteria oxidation is much faster than real rate in varnish formation, however, it should be noted that different kinds of bacteria might have different oxidation rates, thus totally eliminating the contribution of bacteria in the formation of rock varnish is not reasonable. Previous researches focused on the mineral surface catalysis of clay minerals but neglected the existence of metal oxides (Garvie et al., 2008; Goldsmith et al., 2014), since the former is the dominant part of rock varnish. However, in fact, metal oxides demonstrate better ability in accelerating the Mn(II) oxidation than clay minerals (Wilson, 1980; Davies and Morgan, 1989; X. Wang et al., 2015; Y. Wang et al., 2015; Lan et al., 2017). In laboratory, we conducted experiments to simulate photo-oxidation of Mn(II) catalyzed by different metal oxide minerals. With an initial Mn(II) concentration of 14 mM similar to that of dust, Mn(II) oxidation rate is slow as 0.31 $μM_{Mn} h^{-1}$ in light system without minerals. This rate can be promoted to 0.65–2.47 $μM_{Mn} h^{-1}$ when metal oxide minerals were added into the system, and is about 2.10–7.97 times higher in comparison with laboratory homogenous solution oxidation. Goldsmith et al. (2014) estimated that Mn accumulation rate is 320–680 ppm/year in rock varnish, which is 8.88–18.8 times of the homogenous solution oxidation rate in natural settings. The increase proportions are almost on the same order of magnitude. Therefore, this phenomenon indicates the photo-oxidation of Mn (II) catalyzed by semiconducting minerals may play important roles in formation of rock varnish.
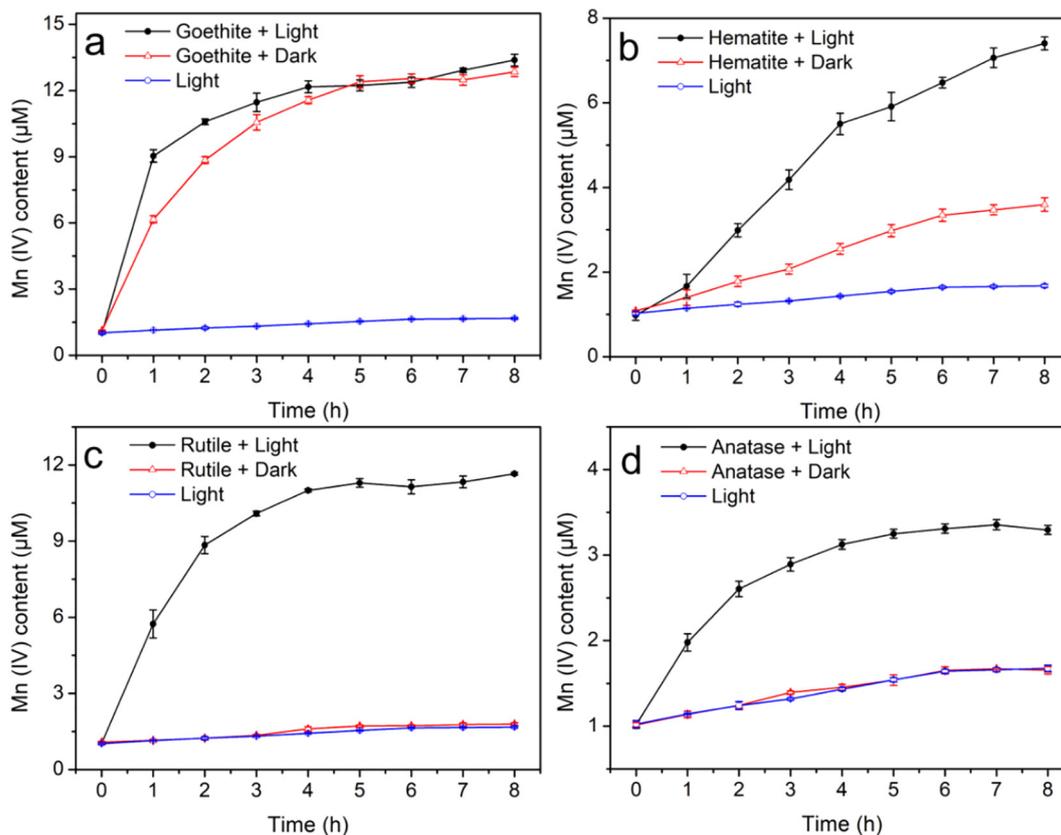
Fig. 15. Curves of Mn(II) oxidation catalyzed by metal oxide minerals. (a) Goethite group; (b) hematite group; (c) rutile group; (d) anatase group.

Table 5
Mn(II) oxidation rates catalyzed by metal oxide minerals after reaction of 8 h.

	Goethite	Hematite	Rutile	Anatase
Blank group ($\mu M_{Mn}\, h^{-1}$)	0.31	0.31	0.31	0.31
Dark group ($\mu M_{Mn}\, h^{-1}$)	2.45	0.51	0.34	0.31
Light group ($\mu M_{Mn}\, h^{-1}$)	2.47	1.14	2.26	0.65

Table 6
Band gap and band edge position of semiconducting minerals in rock varnish with respect to normal hydrogen electrode (NHE, V) and absolute vacuum scale (AVS, eV) at pH 7.

	E_g (eV)	E_V (V)	E_C (V)	E_V (eV)	E_C (eV)	References
Hematite	2.2	2.57	0.37	−7.07	−4.87	Sherman, 2005; Xu and Schoonen, 2000
Goethite	2.6	3.33	0.73	−7.83	−5.23	Sherman, 2005; Xu and Schoonen, 2000
Anatase	3.2	3.8	0.6	−8.3	−5.1	Scanlon et al., 2013
Rutile	3.03	3.33	0.3	−7.83	−4.8	Scanlon et al., 2013
Birnessite	1.82	1.69	−0.13	−6.19	−4.37	Liu et al., 2017

4.4. Implications and limitations

Varnish-like materials were also reported on the surface of other terrestrial planets like Mars (DiGregorio, 2001; Lanza et al., 2015; Arvidson et al., 2016). For a long time, their occurrence was considered to imply the existence of extraterrestrial life since the active biological Mn oxidation process on earth can serve as a good analogy (Marnocha, 2017). However, this evidence can only be suggestive and highly speculative, and a hypothesis of biotic origin of varnish on Mars may encounter with an embarrassing situation that so far no indicative evidence of biological activities on other planets has been reported.
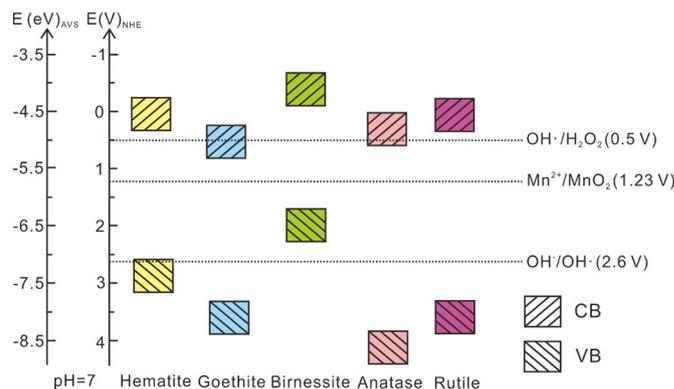

Fig. 16. Diagram of band edge position of semiconducting minerals in rock varnish. Dash lines indicate the redox potential of some half reactions (Pelizzetti and Minero, 1993; Sherman, 2005).

Semiconducting minerals like TiO_2 and Fe_2O_3 were also reported on other terrestrial planet surface (Rieder et al., 1997; Arora et al., 2007) and the occurrence of highly oxidized Mn deposits indicates an aqueous oxidation environment during their formation (Arvidson et al., 2016; Lanza et al., 2016). Therefore, abiotic process such photo-oxidation of Mn may also promote the formation of varnish-like materials on other terrestrial planet surface like Mars.

However, it should be noted that our photo-oxidation model may only account for the formation of varnish in desert regions. Although arid and semi-arid regions are most famous sites for the occurrence of varnish, rock varnish in places where there is no strong solar light irradiation has also been reported, like Antarctica (Dorn et al., 1992), Iceland (Douglas, 1987), caves (Spilde et al., 2006), humid regions (Krinsley et al., 2012; Dorn et al., 2012), etc. Other kinds of Mn coatings like Mn cutan in subsurface regions and Mn dendrite in bedding surface

of rocks are also very common, and there have been different hypotheses for their formation (Chopard et al., 1991; Huang et al., 2008). Furthermore, there could be some competing processes with photo-reduction after the formation of Mn oxides in rock varnish (e.g., Sherman, 2005). Therefore, the photo-oxidation model may account for the formation of varnish together with other pathways.

5. Conclusion

Hypothesis of photo-oxidative formation of Mn oxides in rock varnish was proposed based on geological and laboratory evidence. Field observation reveals close relationship between the occurrence of rock varnish and irradiation of sunlight. The porous structure of varnish can promote the absorption of solar light and intrusion of water. The elements enrichment patterns indicate an aqueous system during its formation and the enrichment of Ce in varnish suggests a strong oxidizing environment in its origin. During varnish formation, wetting effect of rainfall and dew on soil dust gives rise to soluble Mn(II), and metal oxide minerals can accelerate abiotic Mn(II) oxidation through photocatalysis to form solid phase. Under illumination, ROSs such as $^1O_2$ and OH· with strong oxidizing capability are generated through photocatalysis of varnish suspension. Experimental simulation shows different metal oxide minerals can greatly promote Mn(II) oxidation through photocatalysis when compared with homogenous solution oxidation. All these lines of evidence suggest light-induced abiotic process may play important roles in the formation of rock varnish together with other abiotic and biotic pathways.

Acknowledgements

References

Alibo, D.S., Nozaki, Y., 1999. Rare earth elements in seawater: particle association, shale-normalization, and Ce oxidation. Geochim. Cosmochim. Acta 63, 363–372.

Arora, A.K., Tomar, V., Aarti, N., Venkateswararao, K.T., Kamaluddin, N., 2007. Hematite-water system on Mars and its possible role in chemical evolution. Int. J. Astrobiol. 6, 267–271.

Arvidson, R.E., Squyres, S.W., Morris, R.V., Knoll, A.H., Gellert, R., Clark, B.C., Catalano, J.G., Jolliff, B.L., Mclennan, S.M., Herkenhoff, K.E., VanBommel, S., Mittlefehldt, D.W., Grotzinger, J.P., Guinness, E.A., Johnson, J.R., Bell, J.F., Farrand, W.H., Stein, N., Fox, V.K., Golombek, M.P., Hinkle, M.A.G., Calvin, W.M., De Souza Jr, P.A., 2016. High concentrations of manganese and sulfur in deposits on Murray Ridge, Endeavour Crater. Mars. Am. Mineral. 101, 1389–1405.

Billy, C., Blanc, P., 1982. Synthèse de carbonate et oxyde de manganèse par voie bactérienne. C. R. Acad. Sci. 295, 303–305.

Broecker, W.S., Liu, T., 2001. Rock varnish: recorder of desert wetness? GSA Today 1, 4–10.

Brookins, D.G., 1988. Eh-pH Diagrams for Geochemistry. Springer, Berlin.

Chopard, B., Herrmann, H.J., Vicsek, T., 1991. Structure and growth mechanism of mineral dendrites. Nature 353, 409–412.

Chukanov, N.V., 2014. Infrared Spectra of Mineral Species. Springer, Berlin.

Davies, S.H.R., Morgan, J.J., 1989. Manganese(II) oxidation kinetics on metal oxide surfaces. J. Colloid Interface Sci. 129, 63–77.

DiGregorio, B.E., 2001. Rock varnish as a habitat for extant life on Mars. In: Hoover, R.B., Levin, G.V., Paepe, R.R., Rozanov, A.Y. (Eds.), Instruments, Methods, and Missions for Astrobiology IV, pp. 120–130.

Djomgoue, P., Njopwouo, D., 2013. FT-IR spectroscopy applied for surface clays characterization. J. Surf. Eng. Mater. Adv. Technol. 3, 275–282.

Dorn, R.I., 1991. Rock varnish. Am. Sci. 79, 542–553.

Dorn, R.I., 1998. Rock Coatings. Elsevier, Amsterdam.

Dorn, R.I., 2007. Rock varnish. In: David, J.N., Sue, J.M. (Eds.), Geochemical Sediments and Landscapes. Wiley-Blackwell, pp. 246–297.

Dorn, R.I., 2008. In: Nash, D.J., McLaren, S.J. (Eds.), Rock Varnish in Geochemical Sediments and Landscapes. Blackwell Publishing Ltd, Oxford, UK, pp. 246–297 Chapter 8.

Dorn, R.I., 2009. Desert rock coatings. In: Parsons, A.J., Abrahams, A.D. (Eds.), Geomorphology of Desert Environments. Springer, Amsterdam, pp. 153–186.

Dorn, R.I., DeNiro, M.J., 1985. Stable carbon isotope ratios of rock varnish organic matter: a new paleoenvironmental indicator. Science 227, 1472–1474.

Dorn, R.I., Krinsley, D.H., 2011. Spatial, temporal and geographic considerations of the problem of rock varnish diagenesis. Geomorphology 130, 91–99.

Dorn, R.I., Oberlander, T.M., 1981. Microbial origin of desert varnish. Science 213, 1245.

Dorn, R.I., Oberlander, T.M., 1982. Rock varnish. Prog. Phys. Geogr. 6, 317–367.

Dorn, R.I., Krinsley, D.H., Liu, T.Z., Anderson, S., Clark, J., Cahill, T.A., Gill, T.E., 1992. Manganese-rich rock varnish does occur in Antarctica. Chem. Geol. 99, 289–298.

Dorn, R.I., Krinsley, D.H., Ditto, J., 2012. Revisiting Alexander von Humboldt's initiation of rock coating research. J. Geol. 120, 1–14.

Douglas, G.R., 1987. Manganese-rich rock coatings from Iceland. Earth Surf. Process. Landf. 12, 301–310.

Edwards, H.G.M., Moody, C.A., Villar, S.E.J., Mancinelli, R., 2004. Raman spectroscopy of desert varnishes and their rock substrata. J. Raman Spectrosc. 35, 475–479.

Engel, C.G., Sharp, R.P., 1958. Chemical data on desert varnish. Geol. Soc. Am. Bull. 69, 273–286.

Eppard, M., Krumbein, W.E., Koch, C., Rhiel, E., Staley, J.T., Stackebrandt, E., 1996. Morphological, physiological, and molecular characterization of actinomycetes isolated from dry soil, rocks, and monument surfaces. Arch. Microbiol. 166, 12–22.

Faria, D.L.A.D., Silva, S.V., Oliveira, M.T.D., 1997. Raman microspectroscopy of some iron oxides and oxyhydroxides. J. Raman Spectrosc. 28, 873–878.

Francis, C.A., Co, E.M., Tebo, B.M., 2001. Enzymatic manganese(II) oxidation by a marine α-proteobacterium. Appl. Environ. Microbiol. 67, 4024–4029.

Frank, O., Zukalova, M., Laskova, B., Kürti, J., Koltai, J., Kavan, L., 2012. Raman spectra of titanium dioxide (anatase, rutile) with identified oxygen isotopes (16, 17, 18). Phys. Chem. Chem. Phys. 14, 14567–14572.

Garvie, L.A.J., Burt, D.M., Buseck, P.R., 2008. Nanometer-scale complexity, growth, and diagenesis in desert varnish. Geology 36, 215–218.

Georgiou, C.D., Sun, H.J., Mckay, C.P., Grintzalis, K., Papapostolou, I., Zisimopoulos, D., Panagiotidis, K., Zhang, G., Koutsopoulou, E., Christidis, G.E., Margiolaki, I., 2015. Evidence for photochemical production of reactive oxygen species in desert soils. Nat. Commun. 6, 7100.

Goldsmith, Y., Stein, M., Enzel, Y., 2014. From dust to varnish: geochemical constraints on rock varnish formation in the Negev Desert, Israel. Geochim. Cosmochim. Acta 126, 97–111.

Hem, J.D., 1972. Chemical factors that influence the availability of iron and manganese in aqueous systems. Geol. Soc. Am. Bull. 83, 443–450.

Hemley, R.J., 1987. Pressure dependence of Raman spectra of SiO_2 polymorphs: α-quartz, coesite, and stishovite. In: Manghnani, M.H., Syono, Y. (Eds.), High-pressure Research in Mineral Physics. American Geophysical Union, Washington, D.C., pp. 347–359.

Huang, L., Hong, J., Tan, W.F., Hu, H.Q., Liu, F., Wang, M.K., 2008. Characteristics of micromorphology and element distribution of iron-manganese cutans in typical soils of subtropical China. Geoderma 146, 40–47.

Julien, C.M., Massot, M., Baddour-Hadjean, R., Franger, S., Bach, S., Pereira-Ramos, J.P., 2003. Raman spectra of birnessite manganese dioxides. Solid State Ionics 159, 345–356.

Julien, C.M., Massot, M., Poinsignon, C., 2004. Lattice vibrations of manganese oxides – part 1. Periodic structures. Spectrochim. Acta A 60, 689–700.

Kim, S.S., Bargar, J.R., Nealson, K.H., Flood, B.E., Kirschvink, J.L., Raub, T.D., Tebo, B.M., Villalobos, M., 2011. Searching for biosignatures using electron paramagnetic resonance (EPR) analysis of manganese oxides. Astrobiology 11, 775–786.

Krinsley, D.H., 1998. Models of rock varnish formation constrained by high resolution transmission electron microscopy. Sedimentology 45, 711–725.

Krinsley, D.H., Dorn, R.I., Tovey, N.K., 1995. Nanometer-scale layering in rock varnish: implications for genesis and paleoenvironmental interpretation. J. Geol. 103, 106–113.

Krinsley, D.H., Dorn, R.I., DiGregorio, B.E., Langworthy, K.A., Ditto, J., 2012. Rock varnish in New York: an accelerated snapshot of accretionary processes. Geomorphology 138, 339–351.

Krinsley, D.H., Ditto, J., Langworthy, K., Dorn, R.I., Thompson, T., 2013. Varnish microlaminations: new insights from focused ion beam preparation. Phys. Geogr. 34, 159–173.

Krinsley, D.H., DiGregorio, B., Dorn, R.I., 2017. Mn-Fe-enhancing budding bacteria in century-old rock varnish, Erie Barge Canal, New York. J. Geol. 125, 317–336.

Krumbein, W.E., 1968. Über den Einfluß der Mikroflora auf die exogene Dynamik (Verwitterung und Krustenbildung). Geol. Rundsch. 58, 333–363.

Krumbein, W.E., Altmann, H.J., 1973. A new method for the detection and enumeration of manganese oxidizing and reducing microorganisms. Helgoländer Meeresun. 25, 347–356.

Krumbein, W.E., Jens, K., 1981. Biogenic rock varnishes of the Negev Desert (Israel) an ecological study of iron and manganese transformation by cyanobacteria and fungi. Oecologia 50, 25–38.

Kwon, K.D., Refson, K., Sposito, G., 2009. On the role of Mn(IV) vacancies in the photoreductive dissolution of hexagonal birnessite. Geochim. Cosmochim. Acta 73, 4142–4150.

Lan, S., Wang, X., Xiang, Q., Yin, H., Tan, W., Qiu, G., Liu, F., Zhang, J., Feng, X., 2017. Mechanisms of Mn(II) catalytic oxidation on ferrihydrite surfaces and the formation of manganese (oxyhydr)oxides. Geochim. Cosmochim. Acta 211, 79–96.

Lanza, N.L., Clegg, S.M., Wiens, R.C., McInroy, R.E., Newsom, H.E., Deans, M.D., 2012. Examining natural rock varnish and weathering rinds with laser-induced breakdown spectroscopy for application to ChemCam on Mars. Appl. Opt. 51, B74–B82.

Lanza, N.L., Fischer, W.W., Wiens, R.C., Grotzinger, J., Ollila, A.M., Cousin, A., Anderson, R.B., Clark, B.C., Gellert, R., Mangold, N., Maurice, S., Le Mouélic, S., Nachon, M., Schmidt, M., Berger, J., Clegg, S.M., Forni, O., Hardgrove, C., Melikechi, N., Newsom, H.E., Sautter, V., 2015. High manganese concentrations in rocks at Gale crater, Mars. Geophys. Res. Lett. 41, 5755–5763.

Lanza, N.L., Wiens, R.C., Arvidson, R.E., Clark, B.C., Fischer, W.W., Gellert, R., Grotzinger, J.P., Hurowitz, J.A., McLennan, S.M., Morris, R.V., Rice, M.S., Bell, J.F., Berger, J.A., Blaney, D.L., Bridges, N.T., Calef, F., Campbell, J.L., Clegg, S.M., Cousin, A., Edgett, K.S., Fabre, C., Fisk, M.R., Forni, O., Frydenvang, J., Hardy, K.R., Hardgrove, C., Johnson, J.R., Lasue, J., Le Mouélic, S., Malin, M.C., Mangold, N., Martìn-Torres, J., Maurice, S., McBride, M.J., Ming, D.W., Newsom, H.E., Ollila, A.M., Sautter, V., Schröder, S., Thompson, L.M., Treiman, A.H., VanBommel, S., Vaniman, D.T., Zorzano, M., 2016. Geophys. Res. Lett. 43, 7398–7407.

Learman, D.R., Wankel, S.D., Webb, S.M., Martinez, N., Madden, A.S., Hansel, C.M., 2011. Coupled biotic–abiotic Mn(II) oxidation pathway mediates the formation and structural evolution of biogenic Mn oxides. Geochim. Cosmochim. Acta 75, 6048–6063.

Legodi, M.A., Waal, D.D., 2007. The preparation of magnetite, goethite, hematite and maghemite of pigment quality from mill scale iron waste. Dyes Pigments 74, 161–168.

Liu, T., 2003. Blind testing of rock varnish microstratigraphy as a chronometric indicator: results on late Quaternary lava flows in the Mojave Desert, California. Geomorphology 53, 209–234.

Liu, T., Broecker, W.S., 2000. How fast does rock varnish grow? Geology 28, 183–186.

Liu, T., Broecker, W.S., 2007. Holocene rock varnish microstratigraphy and its chronometric application in the drylands of western USA. Geomorphology 84, 1–21.

Liu, T., Broecker, W.S., 2008. Rock varnish microlamination dating of late Quaternary geomorphic features in the drylands of western USA. Geomorphology 93, 501–523.

Liu, Y.G., Miah, M.R.U., Schmitt, R.A., 1998. Cerium: a chemical tracer for paleo-oceanic redox conditions. Geochim. Cosmochim. Acta 52, 1361–1371.

Liu, F.F., Li, Y., Ding, H.R., Ding, C., Lu, A.H., 2017. Researches on the band structure of several types of manganese oxides. Bull. Mineral. Petrol. Geochem. 36, 476–482 (In Chinese with English abstract).

Lu, A., Li, Y., Ding, H., Xu, X., Li, Y., Ren, G., Liang, J., Liu, Y., Hong, H., Chen, N., Chu, S., Liu, F., Li, Y., Wang, H., Ding, C., Wang, C., Lai, Y., Liu, J., Dick, J., Liu, K., Hochella, M.F., 2019. Photoelectric conversion on Earth's surface via widespread Fe- and Mn-mineral coatings. P. Natl. Acad. Sci. USA 116, 9741–9746.

Lucht, K.P., Mendozacortes, J.L., 2015. Birnessite: a layered manganese oxide to capture sunlight for water-splitting catalysis. J. Phys. Chem. C 119, 22838–22846.

Macholdt, D.S., Jochum, K.P., Pöhlker, C., Arangio, A., Foerster, J.D., Stoll, B., Weis, U., Weber, B., Müller, M., Kappl, M., Shiraiwa, M., Kilcoyne, A.L.D., Weigand, M., Scholz, D., Haug, G.H., Al-Amri, A., Andreae, M.O., 2017. Characterization and differentiation of rock varnish types from different environments by microanalytical techniques. Chem. Geol. 459, 91–118.

Malherbe, C., Ingley, R., Hutchinson, I., Edwards, H., Carr, A.S., Harris, L., Boom, A., 2015. Biogeological analysis of desert varnish using portable Raman spectrometers. Astrobiology 15, 442–452.

Mancinelli, R.L., Bishop, J.L., De, S., 2002. Magnetite in desert varnish and applications to rock varnish on Mars. Lunar Planet. Sci. 33, 1046.

Marnocha, C.L., 2017. Rock coatings and the potential for life on Mars. Elements 13, 187–191.

McKeown, D.A., Post, J.E., 2001. Characterization of manganese oxide mineralogy in rock varnish and dendrites using X-ray absorption spectroscopy. Am. Mineral. 86, 701–713.

Morgan, J.J., 2005. Kinetics of reaction between O_2 and Mn(II) species in aqueous solutions. Geochim. Cosmochim. Acta 69, 35–48.

Northup, D.E., Snider, J.R., Spilde, M.N., Porter, M.L., van de Kamp, J.L., Boston, P.J., Nyberg, A.M., Bargar, J.R., 2010. Diversity of rock varnish bacterial communities from Black Canyon, New Mexico. J. Geophys. Res. 115, G002007.

Ohsaka, T., Izumi, F., Fujiki, Y., 1978. Raman spectra of anatase, TiO_2. J. Raman Spectrosc. 7, 321–324.

Palmer, F.E., Staley, J.T., Murray, R.G.E., Counsell, T., Adams, J.B., 1986. Identification of manganese-oxidizing bacteria from desert varnish. Geomicrobiol J. 4, 343–360.

Pelizzetti, E., Minero, C., 1993. Mechanism of the photo-oxidative degradation of organic pollutants over TiO_2 particles. Electrochim. Acta 38, 47–55.

Perry, R.S., Adams, J.B., 1978. Desert varnish: evidence for cyclic deposition of manganese. Nature 276, 489–491.

Perry, R.S., Kolb, V.M., 2004a. From Darwin to Mars: desert varnish as a model for preservation of complex (bio)chemical systems. In: Spie International Symposium on Optical Science & Technology. vol. 5163. pp. 136–144.

Perry, R.S., Kolb, V.M., 2004b. Biological and organic constituents of desert varnish: review and new hypotheses. In: Hoover, R.B., Rozanov, A.Y. (Eds.), Instruments, Methods, and Missions for Astrobiology VII, pp. 202–217.

Perry, R.S., Engel, M.H., Botta, O., Staley, J.T., 2003. Amino acid analyses of desert varnish from the Sonoran and Mojave Deserts. Geomicrobiol J. 20, 427–438.

Perry, R.S., Dodsworth, J., Staley, J.T., Engel, M.H., 2004. Bacterial diversity in desert varnish. In: Harris, R.A., Ouwehand, L. (Eds.), Proceedings of the III European Workshop on Exo-astrobiology: Mars: The Search for Life, pp. 259–260.

Post, J.E., 1999. Manganese oxide minerals: crystal structures and economic and environmental significance. In: Proceedings of the National Academy of Sciences of the United States of America. vol. 96. pp. 3447–3454.

Potter, R.M., Rossman, G.R., 1977. Desert varnish: the importance of clay minerals. Science 196, 1446–1448.

Potter, R.M., Rossman, G.R., 1979a. The manganese- and iron-oxide mineralogy of desert varnish. Chem. Geol. 25, 79–94.

Potter, R.M., Rossman, G.R., 1979b. The tetravalent manganese oxides: identification, hydration, and structural relationships by infrared spectroscopy. Am. Mineral. 64, 1199–1218.

Rieder, R., Economou, T., Wanke, H., Turkevich, A., Crisp, J., Bruckner, J., Dreibus, G., McSween, H.Y., 1997. The chemical composition of Martian soil and rocks returned by the mobile alpha proton X-ray spectrometer: preliminary results from the X-ray mode. Science 278, 1771–1774.

Scanlon, D.O., Dunnill, C.W., Buckeridge, J., Shevlin, S.A., Logsdail, A.J., Woodley, S.M., Catlow, C.R., Powell, M.J., Palgrave, R.G., Parkin, I.P., Watson, G.W., Keal, T.W., Sherwood, P., Walsh, A., Sokol, A.A., 2013. Band alignment of rutile and anatase TiO_2. Nat. Mater. 12, 798.

Schelble, R.T., McDonald, G.D., Hall, J.A., Nealson, K.H., 2005. Community structure comparison using FAME analysis of desert varnish and soil, Mojave Desert, California. Geomicrobiol J. 22, 353–360.

Sherman, D.M., 2005. Electronic structures of iron(III) and manganese(IV) (hydr)oxide minerals: thermodynamics of photochemical reductive dissolution in aquatic environments. Geochim. Cosmochim. Acta 69, 3249–3255.

Smith, B.J., Whalley, W.B., 1988. A note on the characteristics and possible origins of desert varnishes from southeast Morocco. Earth Surf. Process. Landf. 13, 251–258.

Spilde, M.N., Northup, D.E., Boston, P.J., 2006. Ferromanganese deposits in the caves of the Guadalupe Mountains. In: 57th Field Conference, Caves and Karst of Southeastern New Mexico. Geological Society Guidebook, New Mexico, pp. 161–166.

Spilde, M.N., Melim, L.A., Northup, D.E., Boston, P.J., 2013. Anthropogenic lead as a tracer of rock varnish growth: implications for rates of formation. Geology 41, 263–266.

Sterflinger, K., Krumbein, W.E., Lellau, T., Rullkotter, J., 1999. Microbially mediated orange patination of rock surfaces. Anc. Biomol. 3, 51–65.

Thiagarajan, N., Lee, C.T.A., 2004. Trace-element evidence for the origin of desert varnish by direct aqueous atmospheric deposition. Earth Planet. Sci. Lett. 224, 131–141.

Umebayashi, T., Yamaki, T., Itoh, H., Asai, K., 2002. Analysis of electronic structures of 3d transition metal-doped TiO_2 based on band calculations. J. Phys. Chem. Solids 63, 1909–1920.

Velev, J., Bandyopadhyay, A., Butler, W.H., Sarker, S., 2005. Electronic and magnetic structure of transition-metal-doped α-hematite. Phys. Rev. B 71, 205208.

Vicenzi, E.P., Grissom, C.A., Livingston, R.A., Weldon-Yochim, Z., 2016. Rock varnish on architectural stone: microscopy and analysis of nanoscale manganese oxide deposits on the Smithsonian Castle, Washington, DC. Herit. Sci. 4, 26.

Von Humboldt, A., Bonpland, A., 1819. Voyage aux Régions Équinoxiales du Nouveau Continent. II. pp. 299–304.

Wang, X., Lan, S., Zhu, M., Gindervogel, M., Yin, H., Liu, F., Tan, W., Feng, X., 2015a. The presence of ferrihydrite promotes abiotic formation of manganese (oxyhydr)oxides. Soil Sci. Soc. Am. J. 79, 1297–1305.

Wang, Y., Wang, Q., Zhan, X., Wang, F., Safdar, M., He, J., 2015b. Visible light driven type II heterostructures and their enhanced photocatalysis properties: a review. Nanoscale 5, 8326–8339.

Wilson, D.E., 1980. Surface and complexation effects on the rate of Mn (II) oxidation in natural waters. Geochim. Cosmochim. Acta 44, 1311–1317.

Xu, Y., Schoonen, M.A.A., 2000. The absolute energy positions of conduction and valence bands of selected semiconducting minerals. Am. Mineral. 85, 543–556.

Xu, J., Sahai, N., Eggleston, C.M., Schoonen, M.A.A., 2013. Reactive oxygen species at the oxide/water interface: formation mechanisms and implications for prebiotic chemistry and the origin of life. Earth Planet. Sci. Lett. 363, 156–167.

Xu, X., Ding, H., Li, Y., Lu, A., Li, Y., Wang, C., 2018. Mineralogical characteristics of Mn coatings from different weathering environments in China: clues on their formation. Mineral. Petrol. 112, 671–683.